

# Neuron

## An Interglomerular Circuit Gates Glomerular Output and Implements Gain Control in the Mouse Olfactory Bulb

### Highlights

- Broadcast of odor concentration signals by DAT+ cells throughout the glomerular layer
- Gain control of OB output by DAT+ cells leads to decorrelated odor representations
- DAT+ cells act on M/T cells via chemical and electrical synapses with ET cells
- ET cells are gatekeepers of glomerular output and control M/T responsiveness

### Authors

Arkarup Banerjee, Fred Marbach, Francesca Anselmi, ..., Priyanka Gupta, Bo Li, Dinu F. Albeanu

### Correspondence

albeanu@cshl.edu

### In Brief

Banerjee, Marbach, et al. report that interglomerular crosstalk by DAT+ cells in the olfactory bulb, acting indirectly via ET cells, gates the glomerular output and implements concentration-dependent gain control of the bulb output, enabling sparse and decorrelated odor representations.



# An Interglomerular Circuit Gates Glomerular Output and Implements Gain Control in the Mouse Olfactory Bulb

Arkarup Banerjee,<sup>1,2,5</sup> Fred Marbach,<sup>1,2,5</sup> Francesca Anselmi,<sup>1</sup> Matthew S. Koh,<sup>1,2</sup> Martin B. Davis,<sup>1</sup> Pedro Garcia da Silva,<sup>1,3</sup> Kristen Delevich,<sup>1,2</sup> Hassana K. Oyibo,<sup>1,2</sup> Priyanka Gupta,<sup>1,4</sup> Bo Li,<sup>1,2</sup> and Dinu F. Albeanu<sup>1,2,\*</sup>

<sup>1</sup>Cold Spring Harbor Laboratory, Cold Spring Harbor, NY 11724, USA

<sup>2</sup>Watson School of Biological Sciences, Cold Spring Harbor, NY 11724, USA

<sup>3</sup>Champalimaud Neuroscience Programme, Champalimaud Centre for the Unknown, Lisbon 1400-038, Portugal

<sup>4</sup>National Centre for Biological Sciences, Tata Institute of Fundamental Research, Bangalore 560065, India

<sup>5</sup>Co-first author

\*Correspondence: [albeanu@cshl.edu](mailto:albeanu@cshl.edu)

<http://dx.doi.org/10.1016/j.neuron.2015.06.019>

## SUMMARY

Odors elicit distributed activation of glomeruli in the olfactory bulb (OB). Crosstalk between co-active glomeruli has been proposed to perform a variety of computations, facilitating efficient extraction of sensory information by the cortex. Dopaminergic/GABAergic cells in the OB, which can be identified by their expression of the dopamine transporter (DAT), provide the earliest opportunity for such crosstalk. Here we show in mice that DAT+ cells carry concentration-dependent odor signals and broadcast focal glomerular inputs throughout the OB to cause suppression of mitral/tufted (M/T) cell firing, an effect that is mediated by the external tufted (ET) cells coupled to DAT+ cells via chemical and electrical synapses. We find that DAT+ cells implement gain control and decorrelate odor representations in the M/T cell population. Our results further indicate that ET cells are gatekeepers of glomerular output and prime determinants of M/T responsiveness.

## INTRODUCTION

Variation in stimulus intensity far surpasses the output range (firing rate) of individual neurons. To encode stimuli across a wide intensity range (Vickers, 2000), sensory systems employ gain control mechanisms, trading off sensitivity and resolution to regulate their output in accordance with the expected variation in inputs. The quest to find circuit motifs that mediate gain control has driven a large body of research in various sensory systems, including olfaction (Carandini and Heeger, 1994, 2012; Nikolaev et al., 2013; Ohshiro et al., 2011; Olsen et al., 2010; Robinson and McAlpine, 2009).

Odors are detected in the nasal epithelium by olfactory sensory neurons (OSNs) that project to the olfactory bulb (OB), forming a precise layout of distinct input nodes called glomeruli (Mombaerts, 2006; Shepherd, 1972; Soucy et al., 2009). Each

glomerulus receives input from OSNs expressing a given receptor type, out of a repertoire of ~1,100 in the mouse (Buck and Axel, 1991; Mombaerts et al., 1996). A given odor activates a select combination of odorant receptors, triggering activity of multiple glomeruli across the surface of the bulb. Individual M/T cells integrate signals across several co-active glomeruli via interneurons in the glomerular, external plexiform (EPL), and granule cell layers. Despite the diversity of interneuron populations in the mammalian OB, surprisingly little is known about their influence on M/T cell dynamics in vivo.

Increasing odor concentration results not only in increased response amplitudes of individual glomeruli, but also in the activation/suppression of new glomeruli (Bozza et al., 2004; Meister and Bonhoeffer, 2001; Spors et al., 2006). Therefore, gain control mechanisms in the early olfactory circuit are needed to compress the large variation and diversity of glomerular inputs to match the constant dynamic range of individual OB output neurons (M/T cells). Given the spatially distributed nature of odor inputs, bulb micro-circuits need to mediate crosstalk across co-active glomeruli to perform computations such as intensity normalization and population decorrelation (Spors et al., 2012; Wilson, 2013; Wilson and Mainen, 2006). Recently, in the fly and zebrafish olfactory systems, lateral interactions across glomeruli have been shown to implement gain control and help equalize the population activity of projection neurons (Huang et al., 2010; Olsen and Wilson, 2008; Yaksi and Wilson, 2010; Zhu et al., 2013).

In mammals, a class of dopaminergic/GABAergic interneurons, often referred to as short axon (SA) cells, offers the first opportunity for crosstalk between neighboring, as well as distant, glomeruli (Aungst et al., 2003). They receive feed-forward excitatory inputs within individual glomeruli from both excitatory local interneurons (external tufted cells, ET) and OSNs (Aungst et al., 2003). Contrary to their name, SA cells are unique in their ability to extend far-reaching processes, targeting ET cells associated with nearby as well as distant glomeruli located up to 1.5 mm away (~25 glomerular diameters) (Aungst et al., 2003; Kiyokage et al., 2010; Kosaka and Kosaka, 2011; Pinching and Powell, 1971).

Recent in vitro studies have shown that SA action on ET cells results in GABAergic hyperpolarization followed by

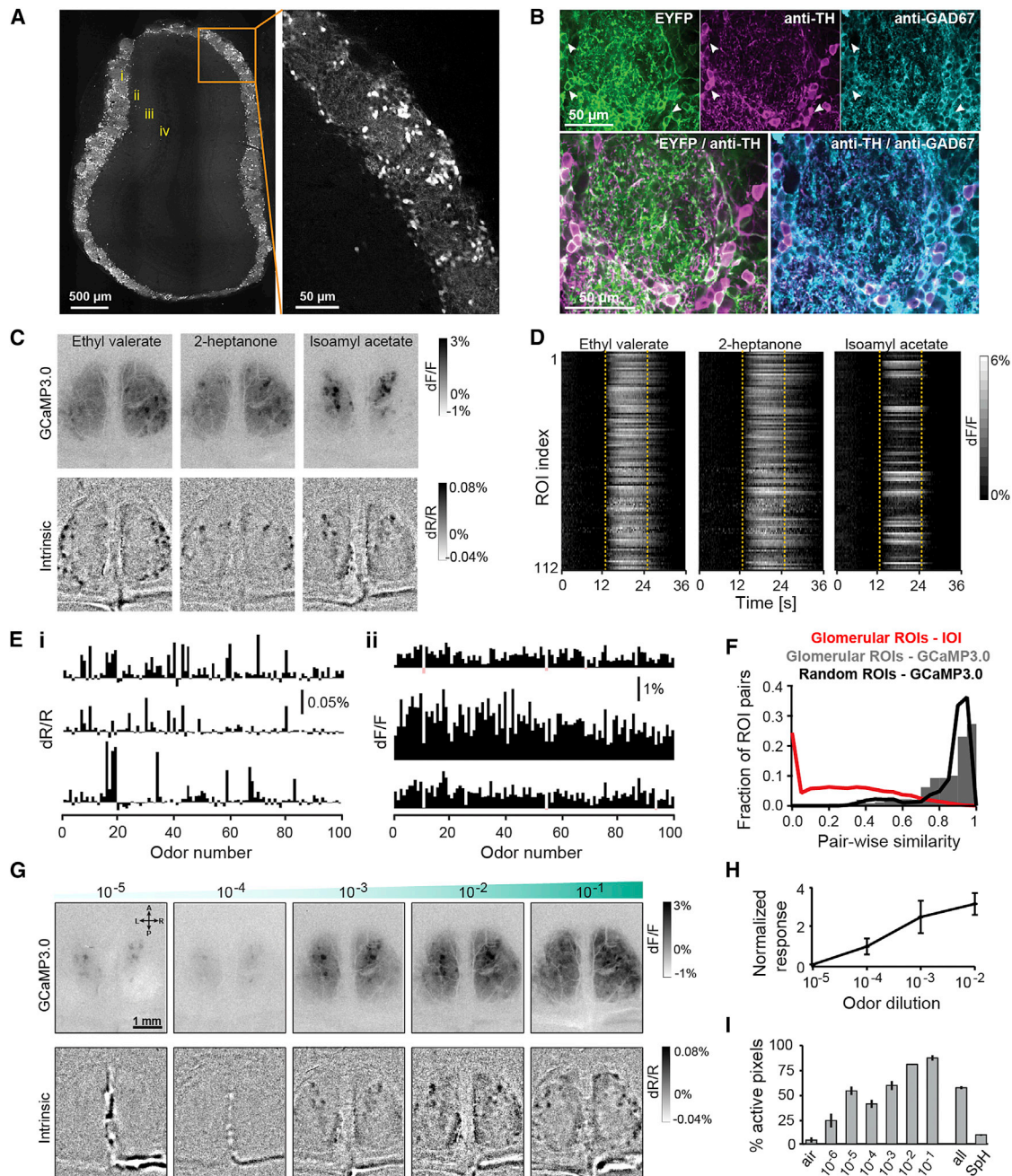


**Figure 1. Long-Range Broadcast of Odor Inputs across the Glomerular Layer**

(A) Expression profile of a DAT-Cre × Ai9 reporter mouse line in a montage of two-photon images of an OB coronal slice. Inset shows DAT+ cells in the glomerular layer. i: glomerular layer; ii: external plexiform layer; iii: mitral cell layer; iv: granule cell layer.

(B) Top: confocal images from a DAT-Cre × Ai32 reporter mouse line, showing ChR2-EYFP fluorescence (left) and immunolabeling with TH antibody (center) and GAD67 antibody (right). Fiduciary marks show individual cell bodies. Bottom left: pseudo-colored merge of ChR2-EYFP (green) and anti-TH (magenta). Bottom right: pseudo-colored merge of anti-TH (magenta) and anti-GAD67 (cyan) staining.

(C) Widefield GCaMP3.0 responses of DAT+ cells (top) and glomerular intrinsic optical imaging (IOI) signals (bottom) in response to ethyl valerate, 2-heptanone, and isoamyl acetate in the same animal.

(D) Time course of GCaMP3.0 signals of all 112 ROIs in response to the same odors from the example shown in (C). ROIs were selected using glomerular outlines estimated from IOI. Dotted lines indicate odor presentation.

(E) Odor response spectra (ORS) of three ROIs monitored via IOI (i) and GCaMP3.0 imaging (ii) to a panel of 100 odors. Rows correspond to different ROIs. Each bar shows the average normalized change in amplitude with respect to baseline (dF/F) for a given odor.

(F) Distribution of ORS pairwise similarity for all ROI pairs within each hemi-bulb. Black line and gray bars, respectively, show similarity of ORS from IOI (14,211 pairs, 8 bulbs, 5 mice; average similarity  $0.31 \pm 0.002$ ) and GCaMP3.0 imaging (5,992 pairs, 3 bulbs, 3 mice; average similarity  $0.83 \pm 0.002$ ). ROIs were selected

(legend continued on next page)

dopamine-mediated (D1) depolarization (Liu et al., 2013; Whitesell et al., 2013). However, the relative excitation versus inhibition conveyed to an M/T cell upon SA activation depends on the interplay between OSN input and the action of other excitatory and inhibitory interneurons (ET and PG cells). Therefore, the net effect of SA action on the M/T output in the intact brain cannot easily be extrapolated from in vitro experiments.

We genetically targeted dopaminergic/GABAergic (DAT+) interneurons in the glomerular layer of the OB. These cells match the known characteristics of SA cells (Aungst et al., 2003; Borisovska et al., 2013; Chand et al., 2015; Kiyokage et al., 2010; Kosaka and Kosaka, 2011; Liu et al., 2013; Tatti et al., 2014; Wachowiak et al., 2013; Whitesell et al., 2013). We asked two questions in this study. First, what is the nature of the signals carried by the DAT+ cells? Second, what is the impact of interglomerular crosstalk mediated by DAT+ cells on the activity of M/T cells? We find that odor responses of DAT+ cells scale with concentration, thereby implementing gain control and decorrelating odor representations in M/T cells. Mechanistically, our results indicate that ET cells are gatekeepers of the glomerular output and prime determinants of M/T cell activity.

## RESULTS

### Genetic Targeting of Dopaminergic/GABAergic Cells in the OB Using DAT-Cre Mice

We used genetically engineered mice (DAT-Cre) that express Cre recombinase under the control of the dopamine transporter (DAT) promoter (Zhuang et al., 2005) to target expression of a genetically encoded calcium indicator (GCaMP3.0), or optogenetic modulators (channelrhodopsin2, ChR2, and halorhodopsin, NpHR3.0) to dopaminergic cells in the OB. DAT-Cre mice were either crossed to Cre-dependent mouse lines to specifically express tdTomato (Ai9), ChR2-EYFP (Ai32), GCaMP3.0 (Ai38) or injected with adeno-associated viruses (AAV) carrying a FLEXed transgene.

The targeted DAT+ cells were located in the glomerular layer (Figure 1A), consistent with previous studies (Kiyokage et al., 2010; Kosaka and Kosaka, 2011; Liu et al., 2013; Whitesell et al., 2013). Focal injection of AAV2.9-EF1a-DIO-ChR2-EYFP in DAT-Cre mice labeled somata near the injection site, as well as processes of variable length extending up to ~1.3 mm away ( $n = 2$  bulbs; Figure S1A; Kiyokage et al., 2010; Kosaka and Kosaka, 2011). Dual immunolabeling in OB slices of DAT-Cre  $\times$  Ai32 mice showed that 85% of EYFP-expressing neurons were TH+. Further, 96% of all TH+ neurons were also GAD67+ (Figure 1B; Kiyokage et al., 2010; Kosaka and Kosaka, 2011). Similarly, in DAT-Cre mice injected with AAV2.9-EF1a-DIO-

ChR2-EYFP, we observed 91% overlap between EYFP+ and TH+ neurons (Figure S1B), corroborating the above results. Consistent with previous reports, we did not find significant overlap (<6%) between DAT+ cells and vGluT2+ (glutamatergic) interneurons by comparing the ChR2-EYFP and anti-vGluT2 fluorescence signals (Figures S1C and S1D; Ohmomo et al., 2009).

Taken together, we find that the DAT+ cells are dopaminergic and GABAergic, are localized in the glomerular layer, and extend processes of variable length spanning distances of up to ~20 glomerular diameters. These characteristics have been ascribed to SA cells, an unfortunate misnomer. To avoid confusion, we will refer to the targeted cells as DAT+ cells throughout this manuscript.

### DAT+ Cells Re-distribute Glomerular Signals throughout the Bulb via Long-Range Processes

As a first step toward understanding the functional role of DAT+ cells, we characterized their responses to a diverse panel of odors (Table S1) and a wide range of concentrations (Figures S1I and S1J) using widefield imaging of GCaMP3.0 signals in anesthetized mice. Individual odors elicited distinct glomerular activity patterns, along with a broad, lower amplitude signal, which was present irrespective of the identity of the odor (Figures 1C–1F, S2A, and S2B; Movies S1 and S2). This broad representation of odors by DAT+ cells was in stark contrast to the discrete and sparse odor maps observed in the same animal via intrinsic optical imaging (IOI), a reliable signature of presynaptic glomerular activity (Figures 1C and S2B; Gurden et al., 2006; Soucy et al., 2009). The widespread nature of odor responses in DAT+ cells was also reflected in the strong overlap between odor response spectra of different regions of interest (ROIs) on the bulb surface (Figure 1E). Consequently, responses of any two ROIs chosen randomly or using glomerular outlines identified via IOI were highly similar (Figure 1F). We verified that the broad spatial extent was not due to light scattering by imaging OMP-synaptotrophin mice (Figures 1I and S2 and Supplemental Notes; Bozza et al., 2004). We found that these broad responses were also present in TH-Cre mice (Figures S2J–S2L and Movies S4 and S5, but see Wachowiak et al., 2013; Supplemental Notes).

We hypothesized that the widespread response results from activation of the long-range processes of DAT+ cells associated with only a few odor-activated glomeruli. Two-photon imaging supported this hypothesis: for any given odor we observed odor-specific, focal activation of DAT+ cell bodies associated with only a few select glomeruli (Figures 2A–2D). The odor response spectra of individual DAT+ cell bodies were sparse and highly correlated for cells located around the boundaries

using glomerular outlines estimated from IOI. Red line shows distribution of pairwise similarity of GCaMP3.0 ORS for arbitrarily selected ROIs on the bulb surface (12,626 pairs, 5 bulbs, 3 mice; average similarity  $0.88 \pm 0.001$ ). Error values indicate SEM unless explicitly stated otherwise.

(G) GCaMP3.0 (top) and IOI (bottom) responses to increasing concentrations of valeraldehyde in the same animal. Odor concentrations are reported as nominal dilutions in mineral oil ( $10^{-5}$ ,  $10^{-4}$ ,  $10^{-3}$ ,  $10^{-2}$ ,  $10^{-1}$ ).

(H) Average GCaMP3.0 responses with increasing odor concentrations. Each point represents the average response of all ROI-odor pairs (311 ROIs, 5 bulbs, 6 odors) normalized and subtracted from the corresponding individual responses at the lowest odor concentration ( $10^{-5}$ ).

(I) Average spatial spread of GCaMP3.0 responses as a function of increasing odor concentration. Each bar shows the average for all bulb-odor pairs (dilutions  $10^{-5}$ – $10^{-2}$ : 5 bulbs, 6 odors; dilutions  $10^{-6}$ – $10^{-1}$ : 2 bulbs, 6 odors). “Air” corresponds to baseline response to clean air stimulation, and “all” corresponds to the pooled average spatial spread across all odors and concentrations from widefield imaging of OMP-SpH mice (66 bulb-odor pairs, 2 bulbs).

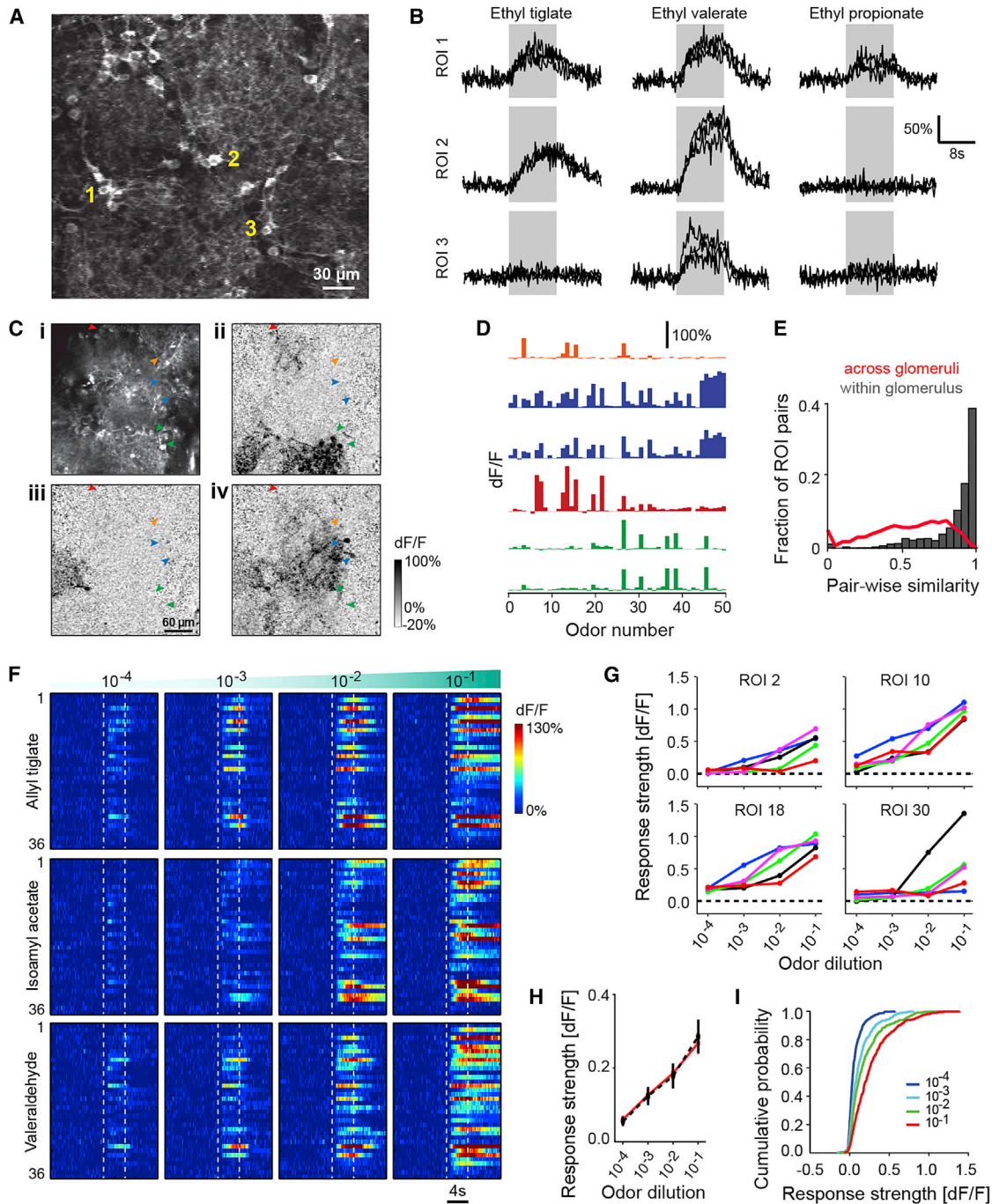


**Figure 2. Responses of Individual DAT+ Cells Are Odor Specific and Scale with Stimulus Concentration**

(A) Two-photon image showing average resting fluorescence of a field of view (FOV) from a DAT-Cre mouse  $\times$  Ai38 reporter mouse line. Numbers denote representative DAT+ cell bodies.

(B) GCaMP3.0 signals (dF/F) of DAT+ cells shown in (A) to ethyl tiglate, ethyl valerate, and ethyl propionate at  $10^{-2}$  oil dilution. Black traces indicate individual trials. Gray band indicates odor presentation.

(C) Two-photon images from a FOV showing average resting fluorescence (i) and odor-evoked dF/F responses (ii–iv) of GCaMP3.0-labeled DAT+ cells around several glomeruli to 2,4,5-trimethyl thiazole (ii), 2-hexanone (iii), and isobutyl propionate (iv). Fiduciary marks indicate cell bodies. Same color arrows indicate DAT+ cells selected around the boundaries of the same glomerulus.

(D) Odor response spectra (ORS) of the DAT+ cells marked in (C) (i) to a panel of 50 odors. Colors indicate putative sister DAT+ cells.

(E) Distribution of ORS similarity for all cell (ROI) pairs within individual FOVs. Gray bars and red line show similarity of ORS corresponding to DAT+ cell bodies selected around the same glomeruli (1,390 pairs; average similarity  $0.86 \pm 0.005$ ) and randomly across glomeruli (9,845 pairs; average similarity  $0.56 \pm 0.003$ ), respectively. 331 ROIs, 50 odors, 4 mice.

(legend continued on next page)

of the same glomerulus, as compared to randomly chosen DAT+ cell pairs (Figures 2D–2E and S2Biii). Widefield imaging of neuropil responses far from the injection site revealed diffuse signals even though individual neuropil responses were sparse and odor specific, similar to DAT+ cell bodies (Figure S3 and Supplemental Notes). We conclude that calcium responses from DAT+ cell neuropil underlie the diffuse component of the widefield signal.

### Odor Responses of DAT+ Cells Increase Monotonically with Concentration

With increasing odor concentration, widefield responses increased in amplitude and spatial spread (Figures 1G–1I and Movies S1 and S2). In contrast, the glomerular IOI and SpH signals remained focal, even when more glomeruli were recruited at a higher concentration (Figure 1G, bottom, and S2C–S2F).

We also monitored responses of individual DAT+ cell bodies across odor concentration with two-photon imaging (Figures 2F–2I). Population analysis of calcium responses pooled across either glomeruli or individual cell bodies showed a monotonic increase in response amplitude with odor concentration (Figures 2H and 2I). Taken together, these results suggest that DAT+ cells broadcast signals throughout the glomerular layer via their far-reaching neuropil, thereby spatially re-distributing glomerular inputs in a concentration-dependent manner.

### Optogenetic Activation of DAT+ Cells Suppresses Spontaneous and Odor-Evoked Firing of M/T Cells

How does the widespread activity of DAT+ cells influence M/T output? We recorded the firing of individual M/T cells using tetrodes while optogenetically stimulating ChR2-expressing DAT+ cells throughout the bulb surface via digital micro-mirror device (DMD)-based patterned illumination (Figure 3A; Dhawale et al., 2010). Systematic mapping of the bulb surface with blue light spots showed long-distance inhibition of the spontaneous firing of M/T units, consistent with a broadcasting role of DAT+ cells (Figure 3B). Decreasing light intensity systematically reduced the overall inhibitory strength while still evoking significant inhibition upon photostimulation as far as 1.5 mm from the recording site (Figures 3B–3C, S4A, and S4B). The observed long-range M/T inhibition may result either from stimulation of distal DAT+ cell bodies that project to the recorded neuron or from antidromic activation of nearby cell bodies upon stimulation of distant axons (Figure 3A, top). However, both of these scenarios support the long-range inhibition of M/T cells by DAT+ cells. Full-field stimulation of ChR2-expressing DAT+ cells also reliably inhibited M/T odor responses. Increasing light intensity resulted in greater suppression of M/T responses, although individual M/T cell inhibition curves differed even for simultaneously recorded cells (Figures 3D and 3E). Furthermore, stimulation with arbitrary

combinations of glomerulus-sized spots also significantly inhibited odor responses of M/T cells (Figures 3F–3G, S4E, and S4F; see Experimental Procedures).

A previous *in vitro* study reported that activating SA cells briefly (20 ms) elicited a bi-phasic excitation-inhibition sequence in ET cells, potentially patterning M/T cell activity (Liu et al., 2013). However, brief light stimulation (10–50 ms) of DAT+ cells *in vivo* resulted in robust suppression of spontaneous activity of M/T cells without any apparent increase in firing rate (Figure S4D). Together, these results suggest a long-range inhibitory drive from DAT+ cells to M/T cells.

### Optogenetic and Pharmacogenetic Silencing of DAT+ Cells Suppresses M/T Firing

ChR2 stimulation provided *in vivo* evidence for the inhibitory action of DAT+ cells. To isolate their contribution to the odor-evoked M/T output, we performed loss-of-function manipulations. We expressed NpHR3.0 in DAT+ cells throughout the dorsal bulb surface and monitored M/T cell activity with tetrodes. We quantified the light-induced change in firing rate (FR) using a change index (CI) defined as  $[(FR_{\text{odor}} - FR_{\text{odor+light}})/(FR_{\text{odor}} + FR_{\text{odor+light}})]$ . Reduced M/T firing upon photostimulation results in  $CI > 0$ , indicating an excitatory action of DAT+ cells, whereas increase in firing rate results in  $CI < 0$ , indicating inhibitory action.

Surprisingly, optogenetic silencing of DAT+ cells by full-field illumination suppressed M/T firing, resulting in positive CIs across all odor concentrations, indicating an excitatory drive (Figures 4A–4C and S5A). Even for the strongest response/stimulus pairs where DAT+ cells were expected to be strongly inhibitory, the average CI was not significantly smaller than zero (Figure 4C). To investigate the spatial extent of M/T cell suppression, we mapped the bulb surface with yellow light spots (Figure 4Di). Light-induced suppression of spontaneous M/T firing decreased with distance from the recording site. We observed inhibitory “cold spots” (Figure S5B) for co-recorded M/T units that were often non-overlapping, in contrast with the broad extent of the inhibitory effect observed in ChR2 experiments. Light stimulation in wild-type mice under identical conditions did not significantly alter M/T firing (Figure S7A).

To confirm the unexpected suppression of M/T cell activity upon optogenetic silencing of DAT+ cells via an alternative approach, we used a viral strategy (Oyibo et al., 2014) to simultaneously label M/T cells with GCaMP3.0 and DAT+ cells with both GCaMP3.0 and DREADDi (Figure S5C; designer receptors exclusively activated by designer drugs; Ferguson et al., 2011). Within this framework, intra-peritoneal injection of the DREADDi ligand, clozapine-N-oxide (CNO), suppresses the activity of cells expressing DREADDi by opening hyperpolarizing K+ channels. We verified that injection of CNO significantly decreased odor responses of DAT+ cells co-expressing DREADDi and GCaMP3.0

(F) GCaMP3.0 signals (dF/F) from 59 DAT+ cells to increasing concentrations of isoamyl acetate, valeraldehyde, and heptanal within the same FOV. Color indicates normalized change in fluorescence with respect to pre-odor baseline. Dotted lines mark odor presentation.

(G) Mean odor response (5 repeats) of four example DAT+ cells in (F) to increasing concentrations of allyl tiglate (blue), isoamyl acetate (cyan), valeraldehyde (green), ethyl valerate (magenta), and heptanal (red).

(H) Mean of odor response from all glomerular ROIs selected (red) and for individual DAT+ cell bodies (dotted black) across five odors, at four different concentrations. 34 glomerular ROIs, 110 DAT+ cells in 3 mice.

(I) Cumulative distribution of DAT+ cells' odor responses across four concentrations ( $n = 110$  DAT+ cells, 3 mice).

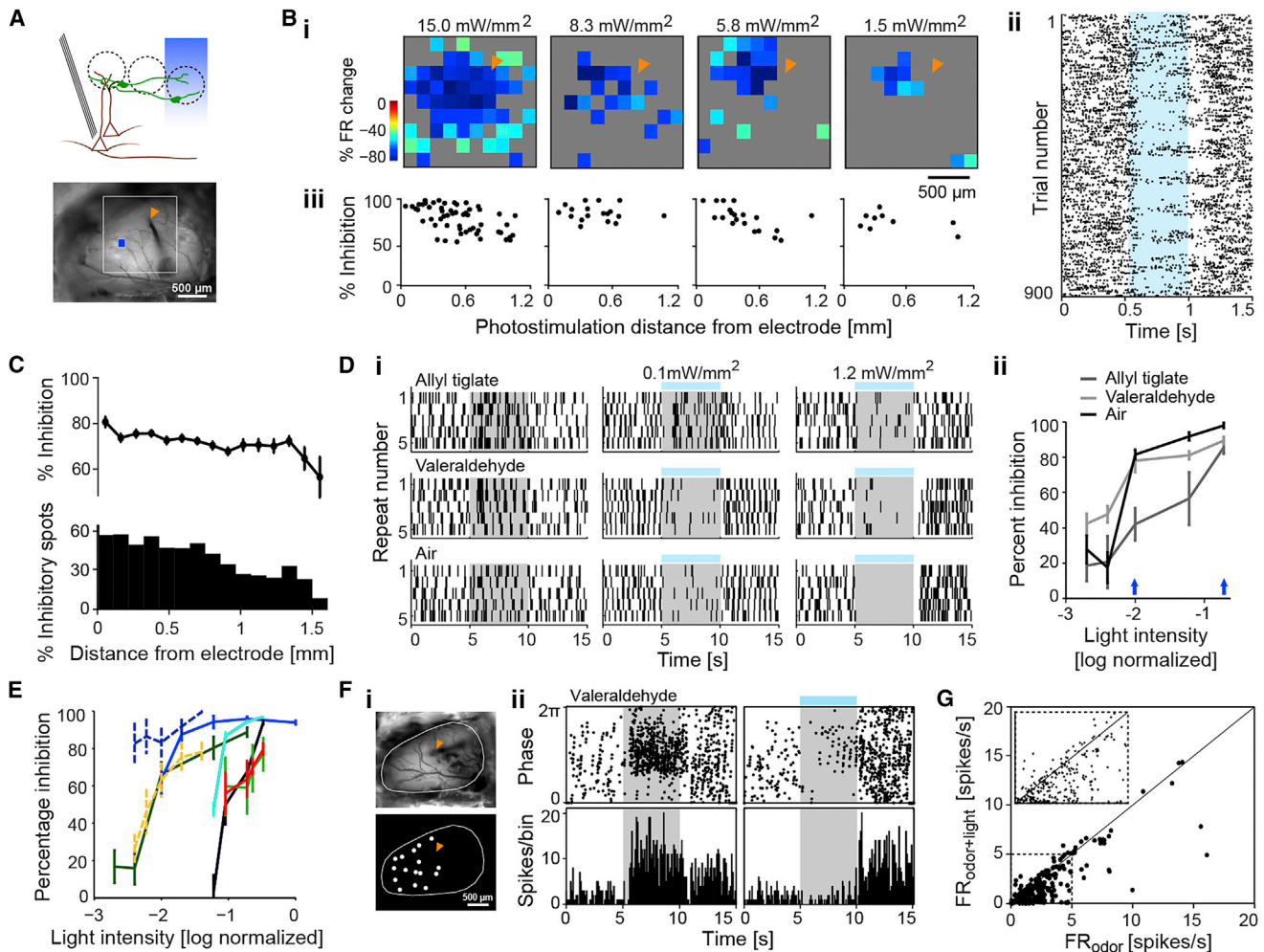


### Figure 3. Photoactivating DAT+ Cells Results in Long-Range Suppression of M/T Cell Firing

(A) Top: schematic of the experiment for optogenetic stimulation of Chr2-expressing DAT+ cells (green) with simultaneous M/T (brown) recordings. Bottom: camera image of the OB, an example spot for photostimulation ( $130 \mu\text{m} \times 130 \mu\text{m}$ ), and fiduciary mark shows location of recording electrodes. Only spots that evoked a significant change from baseline are shown (two-sample t test,  $p < 0.05$ ).

(B) (i) 2D light map of one M/T unit with blue light spots at four different light intensities (15, 8.3, 5.8, 1.5  $\text{mW}/\text{mm}^2$ ). Color indicates percentage change in M/T firing with respect to pre-light stimulation baseline (15 repeats). (ii) Spike raster showing individual trials from the light-mapping session in (i) (15  $\text{mW}/\text{mm}^2$ ). Pixels, from bottom left to top right corner, in the light map are re-ordered as top to bottom rows in the spike raster. All repeats for each pixel are stacked together. Blue band indicates photostimulation. (iii) Strength of light-evoked inhibition as a function of photostimulation distance from the recording site, for the light maps in (i). Each dot represents percentage inhibition from baseline upon stimulation of an individual spot. Only spots that evoked a significant change from baseline are plotted (two-sample t test,  $p < 0.05$ ).

(C) Strength of light-evoked inhibition (top) and fraction of significantly inhibited spots (bottom, two-sample t test,  $p < 0.05$ ) as a function of photostimulation distance from the recording site. Each dot/bar denotes average of all spots from 12 M/T units, 4 mice. Light intensity: 15  $\text{mW}/\text{mm}^2$ .

(D) (i) Spike rasters of an M/T unit upon presentation of allyl tiglate (first row), valeraldehyde (second row), and spontaneous activity (third row) by itself, or with full-field blue light stimulus at two different light intensities (second and third columns). Gray band indicates odor stimulus. Blue line indicates light stimulus. (ii) Percentage inhibition of firing rate ( $(\text{FR}_{\text{odor}} - \text{FR}_{\text{odor+light}}) / \text{FR}_{\text{odor}}$ ) as a function of normalized blue light intensity plotted on log scale for the unit in (i). Blue arrows denote the light intensities corresponding to rasters in (i).

(E) Summary of percentage inhibition versus blue light intensity ( $n = 8$  units, 2 mice). Each line denotes the average percentage inhibition across 5 odors for a single M/T unit. Dotted lines represent M/T units recorded in one mouse and solid lines represent those recorded in a second mouse. Maximum light intensity was 7.9  $\text{mW}/\text{mm}^2$ .

(F) (i) Camera image of the OB (top) and light masks used for photoactivation (bottom) during the recording session shown in (ii). Fiduciary mark (orange) indicates location of recording electrodes. (ii) Peri-stimulus time histograms (PSTH, 500 ms bins) of an example M/T unit in response to valeraldehyde (dilution  $10^{-3}$ ) (left) and valeraldehyde + blue light stimulation (right). Gray band and blue line indicate odor and light stimulus, respectively.

(G) Scatter plot of average firing rates of individual M/T units during odor and odor + light. Points above and below the diagonal, respectively, denote excitation and inhibition of M/T firing. 351 cell-odor pairs, 41 M/T units from 6 mice.

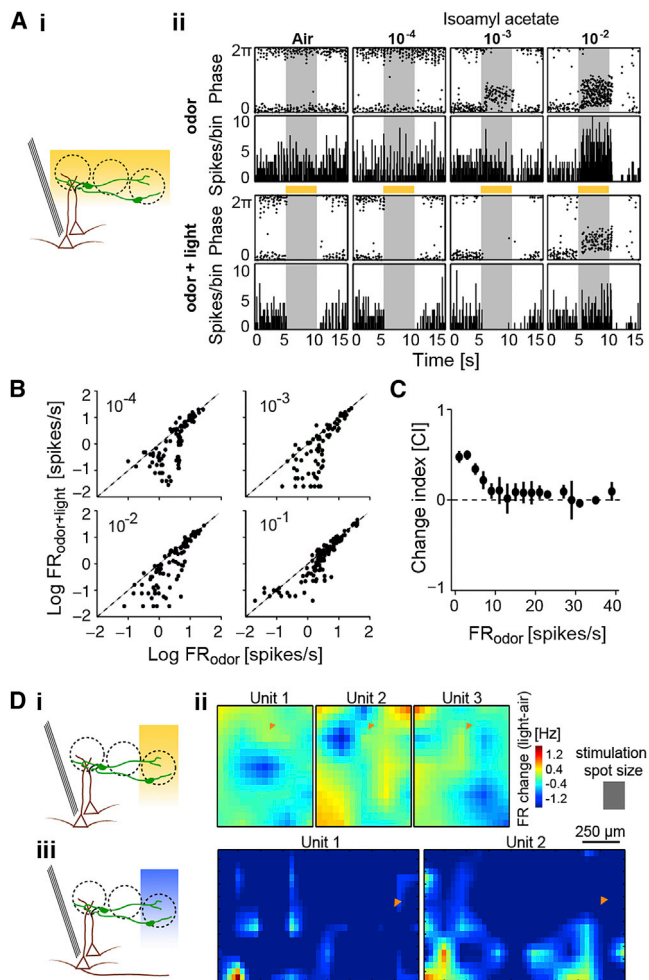


**Figure 4. Optogenetic Silencing of DAT+ Cells Suppresses M/T Cells**

(A) (i) Schematic for in vivo full-field optogenetic inhibition of NpHR3.0-expressing DAT+ cells (green) with simultaneous M/T (brown) recordings. (ii) PSTH (500 ms bins) of an example M/T unit during baseline (air) and increasing concentrations of isoamyl acetate, in the absence (odor) and presence (odor + light) of DAT+ cell suppression (NpHR3.0 stimulation). Yellow bars indicate light stimulus.

(B) Scatter plot of average firing rates of all recorded M/T units during odor and odor + light conditions, at four different odor concentrations.  $10^{-4}$ : 110,  $10^{-3}$ : 94,  $10^{-2}$ : 110,  $10^{-1}$ : 136 cell-odor pairs; 26 M/T units from 12 mice.

(C) Summary plot showing average light-induced effect (change index, CI) for all cell-odor pairs (same as above) as a function of odor-evoked firing rate. CI is calculated as  $[(FR_{\text{odor}} - FR_{\text{odor+light}}) / (FR_{\text{odor}} + FR_{\text{odor+light}})]$ , where  $FR_{\text{odor+light}}$  and  $FR_{\text{odor}}$  correspond to the average odor-evoked firing in the presence and absence of light stimulation, respectively. 450 cell-odor pairs, 26 M/T units, 12 mice.

(D) (i) Schematics of optogenetic inhibition of NpHR3.0-expressing DAT+ cells (green) with simultaneous M/T (brown) recordings. (ii) 2D light maps of three simultaneously recorded M/T units upon optogenetic suppression of NpHR3.0 expressing DAT+ cells by yellow light ( $130 \mu\text{m} \times 130 \mu\text{m}$  size, 500 ms, 50 repeats). Color denotes firing rate change (spikes/s) with respect to pre-light baseline. (iii) 2D light maps of two simultaneously recorded M/T units upon optogenetic activation of Chr2-expressing DAT+ cells by blue light ( $130 \mu\text{m} \times 130 \mu\text{m}$  size, 500 ms, 15 repeats), plotted as in (ii). Fiduciary mark shows location of recording electrodes.

and had no significant effect on M/T odor responses in DAT-Cre negative mice (Figures S5D, S5E, and S7B).

We monitored the responses of M/T cells to odors across a range of concentrations ( $\sim 3$  orders of magnitude) before and after silencing DAT+ cells with DREADDi. Before silencing DAT+ cells, M/T odor responses were characteristically different from responses of DAT+ cells, with diverse concentration response curves and temporal dynamics (Harrison and Scott, 1986; Meredith, 1986; Stopfer et al., 2003). Silencing DAT+ cells reduced both excitatory and inhibitory odor responses of M/T cells, resulting in decreased variance of the M/T odor response distribution (Figures S5F–S5H). Thus, both NpHR3.0 and DREADDi manipulations of DAT+ cells decreased odor responsiveness of M/T cells.

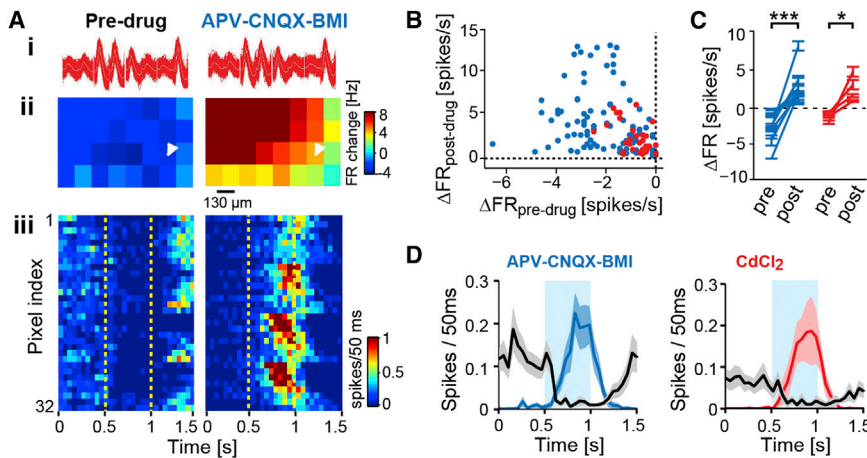
### Chemical and Electrical Synapses between DAT+ Cells and ET Cells Modulate M/T Firing

Surprisingly, both our gain- and loss-of-function experiments resulted in the suppression of M/T activity. Electrical coupling between heterogeneous cell types has been observed in the early sensory systems (Apostolides and Trussell, 2013; Farrow et al., 2013; Huang et al., 2010; Yaksi and Wilson, 2010; Zhu et al., 2013). DREADDi- or NpHR3.0-mediated silencing of DAT+ cells could in principle lead to hyperpolarizing current flow due to electrical coupling, thereby suppressing M/T cells. This scenario is consistent with the suppression of M/T cell responses and the observed local “cold spots” revealed by NpHR3.0 experiments (Figures 4 and S5).

We thus investigated the possibility of electrical coupling between DAT+ cells and M/T cells. Consistent with this idea, the observed M/T suppression upon photo-stimulating Chr2-expressing DAT+ cells reliably turned into excitation upon topical application of glutamatergic and GABAergic antagonists (Figures 5 and S6A). Application of D1 and D2 receptor antagonists in addition to the glutamatergic and GABAergic antagonists resulted in the same effect (Figure S6C). Similar results were observed with topical application of cadmium chloride, which blocks calcium-dependent neurotransmitter release (Figures 5D and S6B). However, even though spontaneous activity of M/T units was reliably blocked, odor-evoked responses were not completely abolished upon drug application (Figure S6D). Despite this caveat, electrical coupling remains the most parsimonious explanation of the observed effect.

To investigate the interaction between DAT+ and M/T cells under more controlled experimental conditions, we performed in vitro whole-cell recordings from mitral cells while photoactivating DAT+ cells. Consistent with a recent study (Whitesell et al., 2013), we found no direct synaptic inhibition onto mitral cells. Surprisingly, we did not find evidence for electrical coupling either (Figures S7 and S8 and Supplemental Notes).

Previous in vitro studies have reported that ET cells are a major source of excitatory input to M/T cells (Gire et al., 2012; De Saint Jan et al., 2009) and also the principal synaptic target of SA cells (Liu et al., 2013; Whitesell et al., 2013). We thus tested the possibility of electrical coupling between DAT+ cells and ET cells. We performed whole-cell recordings from ET cells in acute bulb slices (Figure 6A) while stimulating DAT+ cells expressing Chr2 via full-field blue light stimulation. We observed a robust light-evoked outward current at  $-30$  mV holding potential in ET



(B) Scatter plot showing light-evoked change in firing rate of 15 M/T units during control and drug conditions. Each dot corresponds to a light stimulation spot that significantly modulated firing of the recorded M/T unit in the control condition. Blue and red dots correspond to APV-CNQX-BMI (92 spots, 11 M/T units) and CdCl<sub>2</sub> (32 spots, 4 M/T units) conditions, respectively. Significance was tested using a paired t test for all spots shown before and during drug application (blue dots,  $p < 0.001$ ) and CdCl<sub>2</sub> (red dots,  $p < 0.001$ ).

(C) Summary plot showing light-evoked change in firing rate of all M/T units before and during APV-CNQX-BMI (blue, 11 M/T units, 4 bulbs) and CdCl<sub>2</sub> (red, 4 M/T units, 2 mice) application. \* $p < 0.05$ , \*\*\* $p < 0.001$ , paired t test.

(D) Average time course of firing rate of all recorded M/T units before (black) and during application of APV-CNQX-BMI (blue) or CdCl<sub>2</sub> (red). Only spots that significantly modulated the M/T firing rate in the control condition were included. Shaded bands indicate SEM across M/T units.

### Figure 5. Light-Induced Suppression of M/T Cells by DAT+ Cells Switches to Excitation in the Presence of Synaptic Blockers

(A) (i) Spike waveforms of an example M/T unit from a DAT-Cre mouse injected with AAV2.9-DIO-ChR2-EYFP virus before (left) and after (right) application of drugs. (ii) Example M/T unit shown in (i) showing change in firing upon mapping the OB surface with blue light spots (130  $\mu\text{m} \times 130 \mu\text{m}$ , 15 mW/mm<sup>2</sup>, 15 repeats) before (top) and 30 min after (bottom) bath application of synaptic blockers (APV-CNQX-BMI). Color indicates percentage change in firing with respect to pre-light stimulation baseline. (iii) PSTHs of all spots from the light mapping session in (i), before (left) and after (right) drug application. Pixels, from bottom left to top right corner, in the light map are re-ordered as top to bottom rows in the PSTH. Dotted lines indicate light stimulus. Color indicates firing rate in each 50 ms bin. Fiduciary mark shows location of recording electrodes.

cells, which switched sign to an inward current at more negative potentials ( $< -60$  mV), indicating GABAergic origin, consistent with a recent report (Figure 6B; Whitesell et al., 2013). Furthermore, application of synaptic blockers completely blocked spontaneous EPSCs and abolished the outward current (Figures 6B and 6C). However, at hyperpolarized membrane potentials ( $-90$  mV), application of synaptic blockers altered a fast component of the light-evoked inward current, unmasking a slow-rising component (Figures 6B and 6C), suggesting electrical coupling. We did not observe any appreciable inward current after synaptic block at  $-30$  mV holding potential. This may be because of a residual synaptic outward current due to incomplete drug action masking the much smaller inward gap-junction current (Figure 6Bii, top).

To avoid indirect and residual synaptic effects, we resorted to hyperpolarizing DAT+ cells using NpHR3.0 while recording from ET cells. Upon photostimulation, we observed a slow-rising outward current in ET cells ( $-70$  mV holding potential; Figure 6D) as well as hyperpolarization in current clamp recordings (Figure S8E). In an independent set of experiments, application of synaptic blockers abolished the spontaneous synaptic events in ET cells, but did not alter the yellow-light-induced outward current (Figures 6D and 6E). Together, these results strongly support the existence of gap junctions between DAT+ cells and ET cells in addition to synaptic coupling.

### Gain Control and Decorrelation of Mitral Cell Odor Representations by DAT+ Cells

Gap-junction coupling between DAT+ and ET cells makes it difficult to interpret the results of silencing experiments that rely on hyperpolarization (NpHR3.0 and DREADDi) of DAT+ cells. NpHR3.0 stimulation not only silences the odor-activated

DAT+ cells, but also induces hyperpolarization of ET cells (Figure S8E), a major driving force for M/T firing. This may explain the net decrease in M/T responsiveness, instead of the expected disinhibition of M/T firing (Figures 4 and S5). Therefore, we pursued an alternative strategy (Azim et al., 2014) to specifically ablate DAT+ cells in the OB. We expressed Cre-dependent diphtheria toxin receptor (AAV-FLEX-DTR-GFP) in DAT+ cells. 3 weeks post viral infection, we administered diphtheria toxin (DT) intraperitoneally (see Experimental Procedures), and after 1 week we assessed the effects of this manipulation on DAT+ cells by anti-TH immunohistochemistry in OB slices. On average, the density of TH+ neurons was drastically reduced:  $< 10\%$  TH+ cells on the dorsal OB surface compared to the ventral aspect of the bulb within the same slices (Figure 7A).

We combined DTR/DT-induced ablation of DAT+ cells in the OB with simultaneous optical monitoring of odor responses in mitral cells in DAT-Cre  $\times$  Thy1 GCaMP3.0 mice, which sparsely express GCaMP3.0 in M/T cells (Chen et al., 2012). We used two-photon imaging to chronically monitor mitral cell odor responses to the same stimuli used previously, in either the presence (control condition) or absence (post-ablation, +DT condition) of DAT+ cells across different fields of view (FOV), in the same animal or across individuals. As expected, in the control condition, mitral cells (MCs) showed a wide variety of concentration response curves and temporal dynamics ( $n = 168$  cells, 7 FOVs, 7 mice; Figures 7B–7F). Ablation of DAT+ cells significantly altered the concentration dependence of MC odor responses: most MC concentration response curves scaled monotonically with stimulus intensity (Figures 7B and 7C), and the mean MC odor response amplitude was substantially higher ( $n = 150$  cells, 7 FOVs, 3 mice; Figure 7D).

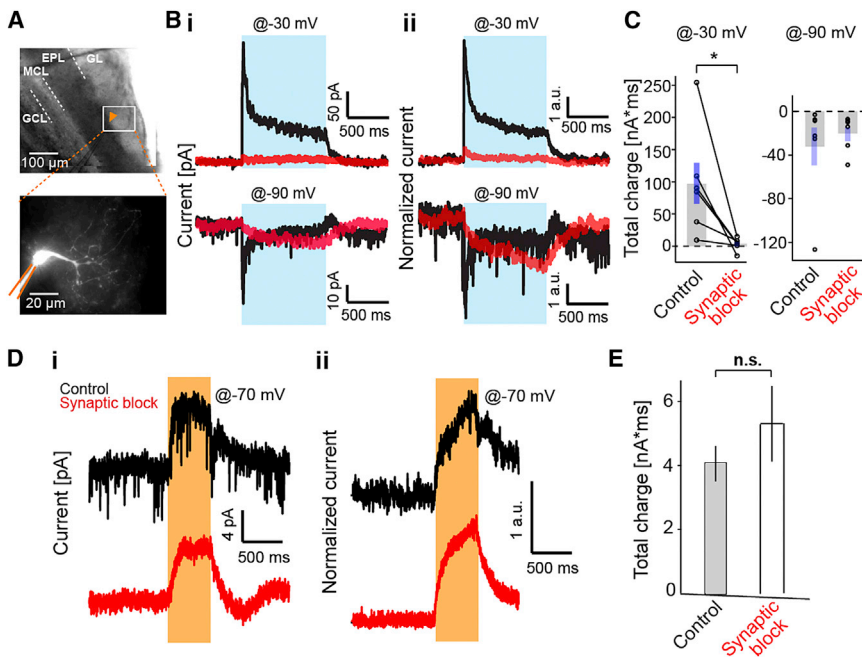


**Figure 6. DAT+ Cells Interact with ET Cells through Both Chemical and Electrical Synapses**

(A) Whole-cell recordings from ET cells upon full-field activation of ChR2-expressing DAT+ cells in acute horizontal OB slices. Top: image of the patch pipette (fiduciary mark) recording from an ET cell in the GL. Bottom: typical morphology of an ET cell filled with Alexa 594 fluorescent dye.

(B) Voltage clamp recordings from ET cells as above. (i) Top: application of synaptic transmission blockers abolishes the light-induced outward current at  $-30$  mV holding potential in a representative ET cell. Black and red traces (average of 10 repeats) represent trials pre- and post-drug application, respectively. Blue bar indicates light stimulation. Bottom: in the same ET cell, the light-induced current reverses polarity at  $-90$  mV holding potential (black trace, average of 10 repeats). Application of synaptic blockers (red trace, average of 10 repeats); (ii) average of light-induced currents of 6 ET cells at  $-30$  mV (top) and  $-90$  mV (bottom) holding potentials, before (black) and after (red) pharmacological block of synaptic transmission. Currents from individual cells are normalized by the average current during the pre-drug light period.

(C) Summary of total light-induced charge in ET cells shown in (B) before and after pharmacological block of synaptic transmission. Average light-induced total charge at  $-30$  mV before ( $98 \pm 32$  nA  $\times$  ms) and after synaptic block ( $3.2 \pm 3.7$  nA  $\times$  ms) was significantly different ( $n = 6$  cells,  $p = 0.037$ , paired t test). Average light-induced total charge at  $-90$  mV was  $-32 \pm 18$  nA  $\times$  ms and  $-20 \pm 6$  nA  $\times$  ms before and after synaptic block, respectively ( $n = 6$  cells).

(D) Voltage clamp traces ( $-70$  mV holding potential) from ET cells upon full-field inactivation of NpHR3.0-expressing DAT+ cells. (i) In an example ET cell, yellow light induces an outward current (top, average of 10 repeats), which persists in the presence of synaptic blockers (bottom, average of 10 repeats). (ii) Average light-induced currents across ET cells in the absence (top,  $n = 8$ ) or in the presence (bottom,  $n = 12$ ) of synaptic blockers. Currents from individual cells are normalized by the average current during the light period.

(E) Total light-induced charge at  $-70$ mV holding potential in the ET cells in the absence ( $4.1 \pm 0.55$  nA\*ms,  $n = 8$  cells) and presence ( $5.3 \pm 1.2$  nA\*ms,  $n = 7$  cells) of synaptic blockers ( $p = 0.37$ , two-sample unpaired t test).

Ablation of DAT+ cells also altered the temporal dynamics of MC responses, substantially reducing both the mean and the variance of onset latency in the odor responses (Figure 7C). Furthermore, the cumulative distribution of MC response strengths across concentrations showed significantly larger variance in the absence of DAT+ cells (Figure 7E; two-sample F test,  $p < 0.001$ ). Therefore, the concentration-dependent inhibition of MCs by DAT+ cells stabilizes not only their mean response amplitude, but also the entire distribution over a wide range of odor concentrations.

To determine whether DAT+ cells implement gain control of MC odor responses, we quantified the slope of the mean MC population response for each FOV as a function of concentration. We observed a substantial rightward shift in the distribution of MC population response slopes post-ablation of DAT+ cells (Figure 7F;  $n = 35$ , 7 FOV for 5 odors, two-sample t test,  $p < 0.01$ ). In addition, for each odor concentration, we observed denser activation of imaged MCs as quantified by a decrease in the population sparseness (Figure 7G; see Experimental Procedures). Computationally, sparsening of neuronal activity has been proposed as an efficient mechanism for decorrelating different inputs. Indeed, the pairwise odor similarity (defined as the correlation coefficient between the neuronal response spectra of odor pairs, pooled across all cells, see Experimental Procedures) was signifi-

cantly higher post-ablation of DAT+ cells compared to control (Figure 7H).

Taken together, our results indicate that DAT+ cells implement gain control by suppressing MC responses with increasing odor concentration, thereby decorrelating MC representations across odors and stimulus intensities.

## DISCUSSION

In this study, we genetically targeted dopaminergic/GABAergic (DAT+) interneurons in the mouse OB (Figure 1). These cells reside in the glomerular layer of the OB and match the known characteristics of short axon cells. DAT+ cells re-distribute focal odor inputs and broadcast long-range signals across the glomerular layer. The spatial spread and amplitude of these responses increase with odor concentration (Figures 1 and 2). DAT+ cells convey local and far-reaching synaptic inhibition to M/T cells indirectly (Figure 3). We find that DAT+ cells modulate the onset dynamics of mitral cells, decrease the gain of M/T population responses, and decorrelate odor representations via concentration-dependent inhibition (Figure 7). Additionally, we provide evidence for electrical coupling between ET and DAT+ cells (Figures 4, 5, and 6). Our results indicate that ET cells are gatekeepers of the glomerulus output and that synaptic and electrical interactions between DAT+ cells and ET cells

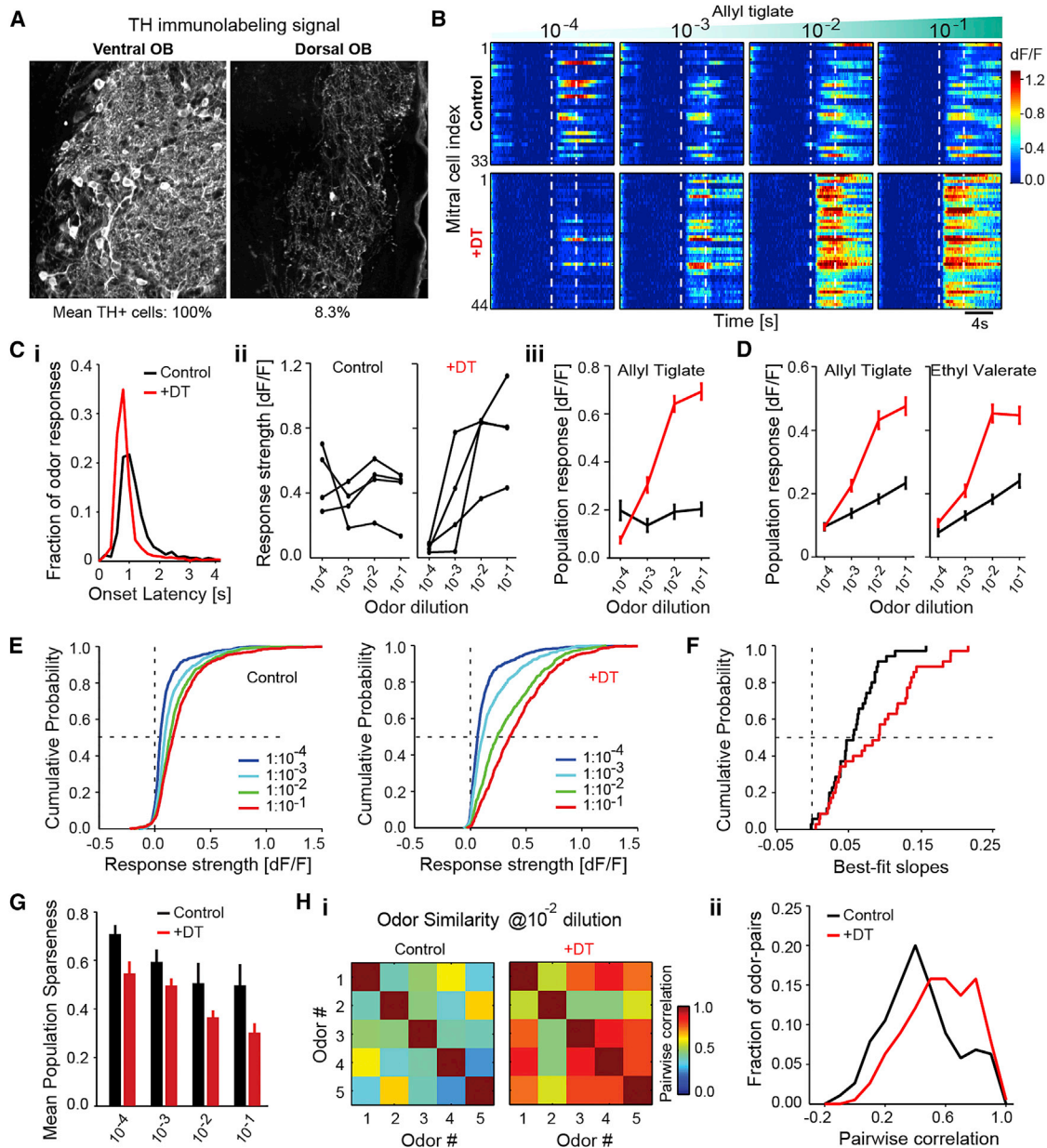


**Figure 7. DAT+ Cells Implement Gain Control and Decorrelate Mitral Cell Odor Responses**

(A) TH+ immunohistochemistry in the olfactory bulb of a DAT-Cre  $\times$  Thy1-GCaMP3.0 mouse injected with AAV2.9-FLEX-DTR-GFP virus on the dorsal aspect of the OB followed by diphtheria toxin (DT) intraperitoneal injection. Confocal images of TH+ signal in two representative FOVs on the ventral (left) and dorsal (right) aspect of a given slice. Average counts of TH+ cells from all dorsal FOVs and from all ventral FOVs in DTR injected mice, normalized by the number of visible glomeruli (100% for control and 8.3% for +DT,  $n = 1,259$  cells, 8 FOVs, 2 mice). Residual signals mostly consisted of neuropil.

(B) Baseline-subtracted, normalized GCaMP3.0 ensemble mitral cell responses to increasing concentrations of allyl tiglate. Top: DAY 0 before injection of DT (control,  $n = 33$  cells). Bottom: different FOV in the same OB on DAY 7 after DT injection (+DT,  $n = 44$  cells). Each row represents an individual mitral cell (ROI) in the same FOV. Color indicates (dF/F). Dotted lines indicate odor presentation (4 s).

(C) (i) Distribution of onset latencies of mitral cell odor responses for control ( $1.55 \text{ s} \pm 1.51 \text{ s}$ ,  $n = 3,660$  cell-odor pairs) and +DT condition ( $1.2 \text{ s} \pm 1.39 \text{ s}$ ,  $n = 3,000$  cell-odor pairs). Numbers denote mean and SD. Both the mean (two-sample  $t$  test,  $p < 10^{-19}$ ) and the variance ( $F$  test,  $p < 10^{-5}$ ) are significantly smaller in the +DT condition. (ii) Odor-evoked response (dF/F) of four example mitral cells from (B) as a function of odor concentration. (iii) Mean odor-evoked response (dF/F) of all mitral cells from (B) as a function of odor concentration for allyl tiglate on day 0 (black,  $n = 33$  cells) and day 7 after DT administration (red,  $n = 44$  cells).

(D) Mean odor-evoked response (dF/F) of all mitral cells pooled across experiments as a function of odor concentration for allyl tiglate and ethyl valerate. Concentration response curves are shown for control (black,  $n = 168$  cells, 7 FOVs, 7 mice) and +DT conditions (red,  $n = 150$  cells, 7 FOVs, 3 mice).

(E) Cumulative distribution of odor response strength of all mitral cells pooled across experiments, to five odors as a function of concentration in the control condition ( $n = 168 \times 5$  cell-odor pairs for each concentration) and after +DT injection ( $n = 150 \times 5$  cell-odor pairs for each concentration).

(legend continued on next page)

tightly regulate the responsiveness of M/T cells to odors (Figure 8).

### Long-Range Crosstalk in the Glomerular Layer

Odors activate distinct patterns of glomeruli that are non-topographically distributed across the OB surface. Interglomerular crosstalk has been proposed to be implemented by a rich diversity of interneurons (PG, PV+, and granule cells), which operate at different stages and spatial scales in the circuit (Kato et al., 2013; Miyamichi et al., 2013; Wilson and Mainen, 2006). Recently, PV+ cells in the EPL have been shown to sample inputs from M/T cell dendrites across  $\sim 250 \mu\text{m}$  and, in turn, provide feedback inhibition to the M/T cells within the same area of reach (Kato et al., 2013; Miyamichi et al., 2013). In contrast, interneurons in the glomerular layer, such as DAT+ cells, receive inputs directly or indirectly from OSNs and are therefore poised to mediate feedforward inhibition of mitral cells (Linster and Cleland, 2009). DAT+ cells offer the first opportunity for crosstalk between distant co-active glomeruli because of their unique ability to transmit long-range signals ( $\sim 1.5 \text{ mm}$ ).

Indeed, we found that the ensemble response of DAT+ cells was odor-indiscriminate and highly correlated across the bulb surface (Figures 1, S2, and Movies S1, S2, and S3). Individual DAT+ cells responded to odors as sparsely as individual glomeruli (Figure S2B). Thus, the high spatial correlation is likely due to the overlapping neuropil from DAT+ cells affiliated with different glomeruli (Figures 2, S2, and S3). This mixing of glomerular inputs by long-range neuropil of DAT+ cells may enable M/T cells to pool inputs from numerous co-active, but spatially distributed, glomeruli. Consistent with this idea, we found that the firing of M/T cells was significantly suppressed upon stimulation of DAT+ cells across a large area on the OB surface (Figure 3).

Thus, from a very early stage in olfactory processing, the output of a glomerulus is not only determined by direct OSN input, but also by signals originating from other glomeruli, similar to reports in *Drosophila* and zebrafish olfactory systems (Huang et al., 2010; Olsen and Wilson, 2008; Olsen et al., 2010; Yaksi and Wilson, 2010; Zhu et al., 2013).

### Gain Control and Decorrelation of the OB Outputs by DAT+ Cells

DAT+ cells receive feed-forward odor inputs, and their activity and spatial spread scales with increasing odor concentration (Figures 1 and 2). What might be the functional relevance of this concentration-dependent and widespread inhibition mediated by DAT+ cells? Individual M/T cells show a wide variety of concentration response curves (Figures 7C and S5G). However, the average population response strength grows modestly

with concentration. Ablating DAT+ cells resulted in significantly steeper concentration response curves for the population as well as individual M/T cells. Further, population responses of M/T cells became denser and more correlated across odors in the absence of DAT+ cells (Figure 7). Our results indicate that DAT+ cells normalize glomerular output through concentration-dependent inhibition, thereby increasing the input dynamic range of the M/T cell population. Consistent with this interpretation, concentration-dependent gain control by DAT+ cells stabilizes not only the mean response amplitude, but also the variance of the response histogram (Figure 7). Further, DAT+ cells sparsen M/T responses, allowing for decorrelated odor representations. Normalization and decorrelation of population responses in the sensory periphery has been suggested to aid separation of stimuli by subsequent cortical areas in various sensory modalities (Barlow, 1961; Luo et al., 2010; Olsen et al., 2010; Vinje and Gallant, 2000). In addition, our results suggest that DAT+ cells are necessary for maintaining the diversity of onset latencies observed in mitral cell odor responses and thus may also be involved in computations other than gain control.

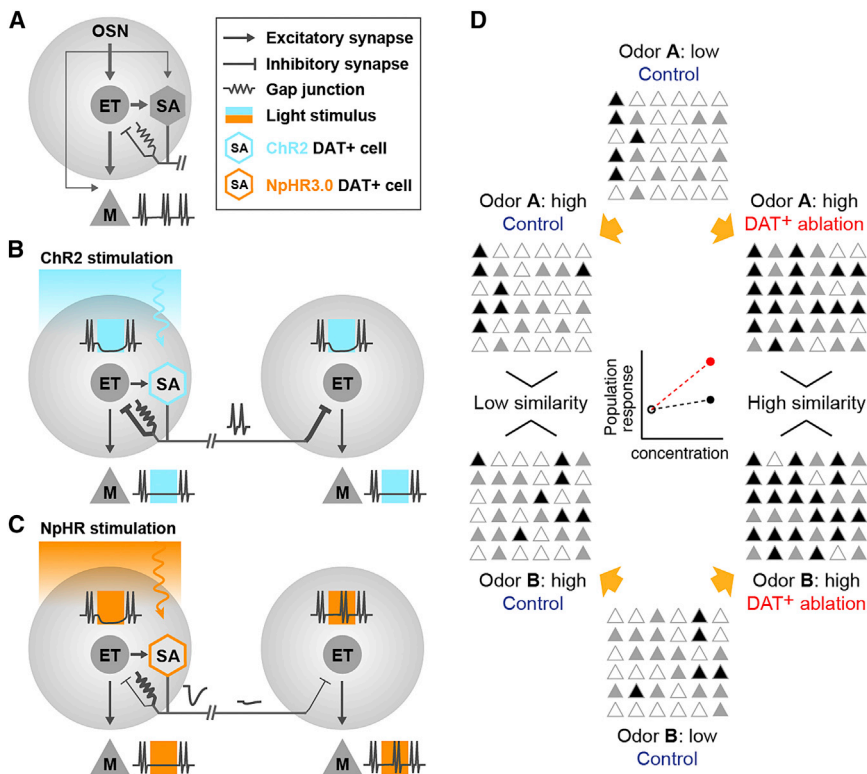
Mechanistically, dense convergence of sparsely responding DAT+ cells from many glomeruli onto individual ET cells would result in sum total inhibition that is proportional to stimulus strength and thus normalize glomerular output. The broadly tuned ensemble responses of DAT+ cells in any local region observed in our widefield imaging experiments (Figure 1), as well as the widespread M/T inhibition upon focal activation of DAT+ cells (Figure 3), are consistent with this scenario. Even with sparser connectivity, long-range broadcast of inhibition by DAT+ cells will result in suppression of weakly responding glomeruli, thereby enhancing the contrast of glomerular activity maps. In either connectivity scenario, the action of DAT+ cells would increase the separability of odor representations in the M/T population. Future experiments combining optogenetic activation of DAT+ cells at glomerular resolution, while monitoring M/T or ET cell activity, will allow direct analysis of the spatial extent, density, and specificity of functional connectivity in the glomerular network.

A recent computational model posited that SA cells implement global normalization of M/T cell responses (Cleland, 2010). This model proposes that SA-ET-SA interactions constitute a small-world network that integrates excitatory inputs across many glomeruli. Thus, within each glomerulus, PG cells inherit a globally averaged signal from ET cells and in turn inhibit M/T cells, ultimately leading to decorrelation of odor representations. This model requires the SA cells to be excitatory (Aungst et al., 2003). Although our results (Figure 6) rule out the proposed mechanism, the function of DAT+ cells is consistent with this model.

(F) Cumulative distribution of slopes of the ensemble mitral cell concentration response curves separately fitted for each FOV and odor, in the control and +DT conditions ( $n = 35$ , 7 FOVs  $\times$  5 odors).

(G) Population sparseness of mitral cell odor representations for each concentration in the control (black,  $n = 168$  cells, 7 FOVs) and +DT conditions (red,  $n = 150$  cells, 7 FOVs). Each bar denotes the mean population sparseness for 5 odors at each concentration.

(H) (i) Matrix of correlation coefficients between the neural response spectra (length of vector = number of recorded neurons) for each odor pair at 1:100 dilution in the control and +DT conditions. (ii) Distribution of pairwise correlation coefficients between all stimulus pairs ( $n = 190$  pairs, 5 odors at 4 concentrations) in the control and +DT conditions (two-sample t test,  $p < 10^{-7}$ ).



centrations increase both the number and amplitude of M/T responses (left). In the absence of DAT+ cells, more M/T cells are recruited (right) and the mean population activity increases more steeply with concentration (red). This results in increased overlap between the population representation of odors A and B. Concentration-dependent lateral inhibition via DAT+ cells decreases the slope (gain) of the mean population activity of M/T cells (black) and reduces overlap between population representations of odors A and B (decorrelation).

### Synaptic and Electrical Coupling in the Glomerular Layer

We found that in addition to synaptic inhibition, DAT+ cells may also influence ET cells via gap junctions (Figures 5 and 6). Multiple aspects of our data suggest the existence of electrical coupling between DAT+ and ET cells. In the presence of synaptic blockers, ChR2 stimulation of DAT+ cells evoked a slow-rising depolarizing current in ET cells (Figures 6B and 6C). Conversely, NpHR3.0 silencing of DAT+ cells resulted in a slow-rising hyperpolarizing current in ET cells, which persisted even after application of synaptic blockers (Figures 6D and 6E). NpHR3.0 silencing *in vivo* also resulted in local suppression of M/T responses (Figure 4D), as would be expected by direct hyperpolarization of ET cells via gap junctions (Figure S8E). Further, DAT+ cell-mediated inhibition of M/T cells switched to excitation upon synaptic block (Figures 5 and S6).

What may be the functional implications of the opposing electrical and synaptic interactions between DAT+ and ET cells? Similar architectures of electrically and synaptically coupled interneurons in the fly and fish olfactory systems have been proposed to bi-directionally modulate the firing of projection neurons by boosting weak odor responses through gap junctions and suppressing strong responses via synaptic inhibition (Huang et al., 2010; Yaksi and Wilson, 2010; Zhu et al., 2013).

### Figure 8. Schematic of the Effect of DAT+ Cell Manipulations on M/T Cell Output

(A) A simplified representation of the basic circuitry within a glomerulus. M/T cell and DAT+ cell firing is primarily driven by excitatory inputs from ET cells, compared to relatively weak contribution of direct OSN inputs. DAT+ cells form inhibitory synapses and gap junctions onto ET cells.

(B) Focal blue-light stimulation of ChR2-expressing DAT+ cells triggers synaptic inhibition of ET cells close by as well as far away. Excitatory drive through gap junctions is weak and readily out-competed by the stronger synaptic inhibition, resulting in net inhibition of ET firing. Loss of excitatory ET drive consequently suppresses M/T cells.

(C) Yellow-light stimulation of NpHR3.0-expressing DAT+ cells hyperpolarizes DAT+ cells and subsequently ET cells due to transmission of light-induced hyperpolarization across gap junctions. The resultant ET inhibition translates into reduced M/T firing as observed in the extracellular recordings. In contrast to (B), the observed inhibition is spatially restricted due to attenuation via passive conductance. Note that both ChR2 and NpHR3.0 stimulation lead to net inhibition of ET cells, albeit via different mechanisms. Under both conditions, net inhibition of ET cells strongly suppresses M/T firing, thereby highlighting the central role played by ET cells in determining OB output.

(D) At low concentrations, odors A and B activate distinct sets of M/T cells (middle). Higher concentrations

increase both the number and amplitude of M/T responses (left). In the absence of DAT+ cells, more M/T cells are recruited (right) and the mean population activity increases more steeply with concentration (red). This results in increased overlap between the population representation of odors A and B.

Concentration-dependent lateral inhibition via DAT+ cells decreases the slope (gain) of the mean population activity of M/T cells (black) and reduces overlap between population representations of odors A and B (decorrelation). Electrical coupling between DAT+ and ET cells may also underlie indirect lateral excitation of M/T cells. The regime in which DAT+ cells could influence ET and M/T cells through gap junctions is, however, constrained by the local spatial scale of effective electrical coupling (Figures 4D and S5B) and the consistently dominant influence of synaptic inhibition observed in our experiments. We did not observe an excitatory effect of DAT+ cells on M/T responses upon genetic ablation of DAT+ cells (Figure 7) or even upon weak ChR2 stimulation of DAT+ cells (Figures 3 and S4). The excitatory influence of DAT+ cells may however be effective under weaker stimulus conditions, which fail to trigger spiking in DAT+ cells, and consequently synaptic inhibition of ET cells.

Intra-glomerular gap junctions in the mammalian OB have also been proposed to synchronize firing of M/T as well as ET cells within the same glomerulus (Christie et al., 2005; Hayar et al., 2005; Schoppa and Westbrook, 2002). Gap junctions may therefore enable ET cells to recruit strong, synchronous, and fast spread of inhibition across the glomerular layer by activating DAT+ cells within the same glomerulus through both electrical and synaptic mechanisms. The roles played by electrical coupling in sensory circuits are just beginning to be explored. In the retina, the extent and potency of electrical coupling can rapidly expand when light levels change (Bloomfield and Völgyi, 2009), in turn modulating the impact of gap junctions on visual

processing. Future studies performed in low-stimulus concentration regimes in awake, behaving animals will elucidate the full extent of the roles played by electrical coupling between DAT+ and ET cells.

### ET Cells Are the Gatekeepers of Glomerular Output

Recent *in vitro* studies (Gire et al., 2012; De Saint Jan et al., 2009) have proposed that ET cells provide the primary excitatory drive to M/T cells within a glomerulus, in contrast with the canonical direct OSN→M/T flow of excitation. These results have been a matter of debate, as they propose an important reconsideration of the basic logic of the bulb circuitry. Several aspects of our data provide the first *in vivo* evidence for the central role of ET cells in determining mitral cell responsiveness.

Odor-evoked spiking in M/T cells was strongly suppressed upon optogenetic activation of DAT+ cells *in vivo*, despite the apparent lack of direct DAT+ to M/T connections (Figures 3 and S8). Given that ET cells are the principal targets of GABAergic inhibition from DAT+ cells (Figures 6 and S8; Whitesell et al., 2013), our *in vivo* results suggest that the majority of odor input to a glomerulus is relayed to M/T cells through ET cells and not directly from the OSNs. Furthermore, optogenetic silencing of DAT+ cells hyperpolarized ET cells *in vitro* (Figure S8E) and greatly reduced M/T odor responses *in vivo* (Figure 4). These results suggest that reduced ET excitability significantly attenuates the odor-induced excitatory drive onto M/T cells (Figure 8). We infer that ET cells act as gatekeepers of glomerular output and regulate the excitability of M/T cells *in vivo*. DAT+ cells suitably target this principal node in the glomerulus, allowing for crosstalk between co-activated glomeruli and strict control of M/T spiking before the EPL or GC interneuronal networks.

In this study, we have not explored the role of dopamine released by DAT+ cells and, in general, the implication of dual neurotransmission in olfactory processing. Preliminary results show that blocking D1 receptors decreases M/T firing (data not shown), suggesting the existence of a synaptic excitatory role of DAT+ cells. Future studies will help understand how the interplay between dopaminergic, GABAergic, and electrical action of DAT+ cells influences OB output.

In summary, our results emphasize that substantial transformation of odor representations occurs in the input layer of the olfactory bulb. These findings open exciting venues to further elucidate the downstream impact of glomerular layer processing on olfactory computations and behavior.

## EXPERIMENTAL PROCEDURES

### Animals and Surgical Methods

All experiments were done in adult mice in accordance with NIH guidelines and CSHL Animal Care and Use Committee. Mice were anesthetized with Ketamine-Xylazine (KX) injections, and body temperature was maintained at 37°C. Craniotomy was performed to expose the dorsal OB and covered with a thin layer of 1.2% agarose. For extracellular recordings, dura mater was removed and a pair of tetrodes (octrodes) was inserted. For acute imaging experiments, a glass cover slide was placed to prevent drying and reduce motion artifacts, whereas a glass window (~3 mm) was implanted for chronic two-photon imaging. DAT-Cre-specific targeting of ChR2, NpHR3.0,

GCaMP3.0, DREADDi, and DTR was achieved using AAV injections at 2–3 sites in the dorsal OB.

### Odor Delivery

Odors were delivered using a custom-made odor machine as described previously (Dhawale et al., 2010). Odors were diluted at 1:100 in mineral oil unless specified otherwise. Throughout the manuscript, concentrations of odors are expressed as nominal dilutions in mineral oil (odor-oil volume ratio). Each odor trial was flanked by air periods, and inter-trial intervals were 15–60 s.

### Photostimulation and Electrical Recordings

Patterned photostimulation of the olfactory bulb using a DLP projector and simultaneous extracellular recordings of M/T cells were performed as described previously (Dhawale et al., 2010). For patch-clamp recordings, signals were recorded with a Multiclamp 700B, low-pass filtered at 10 kHz, and digitized at 10 kHz with an analog-to-digital converter Digidata 1440A, using Clampex 10.2 software (Axon Instruments, Molecular Devices). Anatomical location, *in vitro* fluorescence, spiking characteristics, and morphology visualized by post hoc dye filling were used to identify the cell types.

### Imaging

LED arrays were used to shine blue light for widefield GCaMP3.0 imaging and far red light (780 nm) for intrinsic optical imaging (IOI). Images were acquired at 25 Hz for IOI and 4 Hz for widefield GCaMP3.0 imaging with a Vosskuhler 1300-QF CCD camera. Two-photon imaging (5 Hz) was performed with a custom-built microscope and acquisition software in Labview using a collimated laser beam (930 nm) from a Ti-Sa 80 MHz pulsed laser to backfill a 20× 1.0 NA Olympus objective lens.

### Pharmacology and Ablation of DAT+ Cells

Drug cocktails were superfused over the exposed OB surface 30 min prior to the recording and continuously thereafter. For synaptic block experiments, a cocktail of CNQX, APV, BMI, or CdCl<sub>2</sub> (each at 1 mM) was used. In some experiments (Figure S6C) D1 antagonist SKF83566 hydrobromide and D2 antagonist Sulpiride (1 mM concentration) were also added to block dopaminergic transmission. For DREADDi inactivation experiments (Figure S5), Clozapine-N-oxide (CNO), diluted in saline to a concentration of 4 mg/ml, was injected *i.p.* at a final concentration of 5–10 mg/kg of body weight. Post-CNO imaging session started 30 min after the injection. For genetic ablation of DAT+ cells (Figure 7), DAT-Cre or DAT-Cre × Thy1-GCaMP3.0 mice were injected in the OB with AAV-FLEX-DTR-GFP virus (gift from T. Jessell and E. Azim, Columbia University). 2–3 weeks post injection, either saline or 400 ng of diphtheria toxin (DT, Sigma) was administered *i.p.* Animals were chronically imaged using two-photon microscopy on day 0 (immediately before injecting DT) and 1–2 weeks (days 7–14) subsequently. In some animals, windows were implanted on day 7, 1 week after injection of DT. Data from both conditions were pooled.

### Imaging Analyses

Response strength was quantified as the normalized change in reflectance (dR/R, IOI) or in fluorescence (dF/F, calcium imaging) averaged across repeats. Regions of interest (ROIs) were chosen, and response strength was calculated by averaging over all the pixels in each ROI. The spatial spread of odor responses was calculated by determining the fraction of pixels that responded above 2 SD from the baseline average during air period. Lifetime sparseness was calculated using a modified metric (Willmore and Tolhurst, 2001) to quantify the extent to which a given unit is modulated by different stimuli.

$$LS_i = 1 - \frac{\left(\sum_{j=1}^m \frac{r_j}{m}\right)^2}{\sum_{j=1}^m \frac{r_j^2}{m}}$$

*i* = ROI index for which lifetime sparseness is calculated; *m* = number of odors; *r<sub>j</sub>* = response of the ROI to the odor number *j*. We used, as a similarity

metric, the uncentered correlation coefficient among their odor response spectra (ORS).

$$S^{(A,B)} = \frac{\sum_{j=1}^n r_j^{(A)} \cdot r_j^{(B)}}{\sqrt{\sum_{j=1}^n r_j^{(A)} \cdot r_j^{(A)}} \cdot \sqrt{\sum_{j=1}^n r_j^{(B)} \cdot r_j^{(B)}}}$$

Similarity between ROIs A and B:  $r_j$  = response of ROI to odor  $j$ ;  $n$  = number of odors. Population response was calculated as the mean of the response strengths to a given odor either across all the neurons in a given FOV or all the recorded neurons pooled across experiments. For each odor stimulus, the neuronal response spectrum (NRS) was constructed as a vector containing the response strengths of all the recorded mitral cells pooled across FOVs (length = number of cells) and was used to calculate population sparseness. For each stimulus pair, the Pearson correlation coefficient of these NRSs was calculated to represent odor similarity. All figures denote mean  $\pm$  SEM unless explicitly specified.

### Electrophysiology Analyses

For optogenetic mapping experiments, individual light spots that significantly modulated (“significant spots”) the firing rate (FR) of the recorded unit in either direction compared to the “pre-light” period were assessed using a two-sample  $t$  test ( $p < 0.05$ ). M/T responses were calculated as the mean FR during the baseline, odor, or odor + light periods across all repeats. For each M/T unit, a significance value ( $p$  value) was calculated for every odor and odor + light pair (two-sample  $t$  test) across the repeats. For ChR2 light-mapping experiments with drugs, we identified spots that significantly modulated the FR upon light stimulation during the drug period, same as above. For each significant spot, the light-induced FR change was compared in the control (pre-drug) and drug condition. For a given M/T unit, we calculated the time course of the light-induced response by computing the mean PSTH across all significant spots.

### SUPPLEMENTAL INFORMATION

Supplemental Information includes Supplemental Experimental Procedures, Supplemental Notes, eight figures, one table, and five movies and can be found with this article online at <http://dx.doi.org/10.1016/j.neuron.2015.06.019>.

### AUTHOR CONTRIBUTIONS

A.B., F.M., and D.F.A. conceptualized the study. A.B., F.M., P.G., F.A., M.S.K., B.L., and D.F.A. contributed to the practical design of experiments and analysis. A.B., F.M., P.G.d.S., and D.F.A. performed in vivo OB imaging; A.B. and F.M. in vivo recordings; M.B.D., A.B., and F.M. viral injections and immunohistochemistry; and F.A., M.S.K., and K.D. patching experiments. P.G. implemented hardware instrumentation and acquisition software for in vivo recordings. H.K.O. made the PRV-Cre virus. A.B., F.M., P.G., and D.F.A. wrote the manuscript.

### ACKNOWLEDGMENTS

We would like to thank A. Dhawale, G. Otazu, S. Shea, A. Zador, and A. Kepecs for valuable scientific discussions and input on manuscript preparation, R. Eifert for machine shop assistance, T. Jessel and E. Azim for the gift of DTR virus, M. Luo for the gift of DREADD virus, and members of the Albeanu laboratory for comments on the manuscript. This study was supported by an NIDCD R01 grant, an EMBO Fellowship, CSHL startup funds, Crick-Clay fellowship, and Farish-Gerry fellowship.

Received: January 24, 2014

Revised: April 24, 2015

Accepted: June 10, 2015

Published: July 1, 2015

### REFERENCES

- Apostolides, P.F., and Trussell, L.O. (2013). Regulation of interneuron excitability by gap junction coupling with principal cells. *Nat. Neurosci.* *16*, 1764–1772.
- Aungst, J.L., Heyward, P.M., Puche, A.C., Karnup, S.V., Hayar, A., Szabo, G., and Shipley, M.T. (2003). Centre-surround inhibition among olfactory bulb glomeruli. *Nature* *426*, 623–629.
- Azim, E., Jiang, J., Alstermark, B., and Jessell, T.M. (2014). Skilled reaching relies on a V2a propriospinal internal copy circuit. *Nature* *508*, 357–363.
- Barlow, H. (1961). Possible principles underlying the transformation of sensory messages, W.A. Rosenblith, ed. (Cambridge, MA: MIT Press).
- Bloomfield, S.A., and Völgyi, B. (2009). The diverse functional roles and regulation of neuronal gap junctions in the retina. *Nat. Rev. Neurosci.* *10*, 495–506.
- Borisovska, M., Bensen, A.L., Chong, G., and Westbrook, G.L. (2013). Distinct modes of dopamine and GABA release in a dual transmitter neuron. *J. Neurosci.* *33*, 1790–1796.
- Bozza, T., McGann, J.P., Mombaerts, P., and Wachowiak, M. (2004). In vivo imaging of neuronal activity by targeted expression of a genetically encoded probe in the mouse. *Neuron* *42*, 9–21.
- Buck, L., and Axel, R. (1991). A novel multigene family may encode odorant receptors: a molecular basis for odor recognition. *Cell* *65*, 175–187.
- Carandini, M., and Heeger, D.J. (1994). Summation and division by neurons in primate visual cortex. *Science* *264*, 1333–1336.
- Carandini, M., and Heeger, D.J. (2012). Normalization as a canonical neural computation. *Nat. Rev. Neurosci.* *13*, 51–62.
- Chand, A.N., Galliano, E., Chesters, R.A., and Grubb, M.S. (2015). A distinct subtype of dopaminergic interneuron displays inverted structural plasticity at the axon initial segment. *J. Neurosci.* *35*, 1573–1590.
- Chen, Q., Cichon, J., Wang, W., Qiu, L., Lee, S.-J.R., Campbell, N.R., Destefino, N., Goard, M.J., Fu, Z., Yasuda, R., et al. (2012). Imaging neural activity using Thy1-GCaMP transgenic mice. *Neuron* *76*, 297–308.
- Christie, J.M., Bark, C., Hormuzdi, S.G., Helbig, I., Monyer, H., and Westbrook, G.L. (2005). Connexin36 mediates spike synchrony in olfactory bulb glomeruli. *Neuron* *46*, 761–772.
- Cleland, T.A. (2010). Early transformations in odor representation. *Trends Neurosci.* *33*, 130–139.
- De Saint Jan, D., Hirnet, D., Westbrook, G.L., and Charpak, S. (2009). External tufted cells drive the output of olfactory bulb glomeruli. *J. Neurosci.* *29*, 2043–2052.
- Dhawale, A.K., Hagiwara, A., Bhalla, U.S., Murthy, V.N., and Albeanu, D.F. (2010). Non-redundant odor coding by sister mitral cells revealed by light addressable glomeruli in the mouse. *Nat. Neurosci.* *13*, 1404–1412.
- Farrow, K., Teixeira, M., Szikra, T., Viney, T.J., Balint, K., Yonehara, K., and Roska, B. (2013). Ambient illumination toggles a neuronal circuit switch in the retina and visual perception at cone threshold. *Neuron* *78*, 325–338.
- Ferguson, S.M., Eskenazi, D., Ishikawa, M., Wanat, M.J., Phillips, P.E.M., Dong, Y., Roth, B.L., and Neumaier, J.F. (2011). Transient neuronal inhibition reveals opposing roles of indirect and direct pathways in sensitization. *Nat. Neurosci.* *14*, 22–24.
- Gire, D.H., Franks, K.M., Zak, J.D., Tanaka, K.F., Whitesell, J.D., Mulligan, A.A., Hen, R., and Schoppa, N.E. (2012). Mitral cells in the olfactory bulb are mainly excited through a multistep signaling path. *J. Neurosci.* *32*, 2964–2975.
- Gurden, H., Uchida, N., and Mainen, Z.F. (2006). Sensory-evoked intrinsic optical signals in the olfactory bulb are coupled to glutamate release and uptake. *Neuron* *52*, 335–345.
- Harrison, T.A., and Scott, J.W. (1986). Olfactory bulb responses to odor stimulation: analysis of response pattern and intensity relationships. *J. Neurophysiol.* *56*, 1571–1589.

- Hayar, A., Shipley, M.T., and Ennis, M. (2005). Olfactory bulb external tufted cells are synchronized by multiple intraglomerular mechanisms. *J. Neurosci.* *25*, 8197–8208.
- Huang, J., Zhang, W., Qiao, W., Hu, A., and Wang, Z. (2010). Functional connectivity and selective odor responses of excitatory local interneurons in *Drosophila* antennal lobe. *Neuron* *67*, 1021–1033.
- Kato, H.K., Gillet, S.N., Peters, A.J., Isaacson, J.S., and Komiyama, T. (2013). Parvalbumin-expressing interneurons linearly control olfactory bulb output. *Neuron* *80*, 1218–1231.
- Kiyokage, E., Pan, Y.-Z., Shao, Z., Kobayashi, K., Szabo, G., Yanagawa, Y., Obata, K., Okano, H., Toida, K., Puche, A.C., and Shipley, M.T. (2010). Molecular identity of periglomerular and short axon cells. *J. Neurosci.* *30*, 1185–1196.
- Kosaka, T., and Kosaka, K. (2011). “Interneurons” in the olfactory bulb revisited. *Neurosci. Res.* *69*, 93–99.
- Linster, C., and Cleland, T.A. (2009). Glomerular microcircuits in the olfactory bulb. *Neural Netw.* *22*, 1169–1173.
- Liu, S., Plachez, C., Shao, Z., Puche, A., and Shipley, M.T. (2013). Olfactory bulb short axon cell release of GABA and dopamine produces a temporally biphasic inhibition-excitation response in external tufted cells. *J. Neurosci.* *33*, 2916–2926.
- Luo, S.X., Axel, R., and Abbott, L.F. (2010). Generating sparse and selective third-order responses in the olfactory system of the fly. *Proc. Natl. Acad. Sci. USA* *107*, 10713–10718.
- Meister, M., and Bonhoeffer, T. (2001). Tuning and topography in an odor map on the rat olfactory bulb. *J. Neurosci.* *21*, 1351–1360.
- Meredith, M. (1986). Patterned response to odor in mammalian olfactory bulb: the influence of intensity. *J. Neurophysiol.* *56*, 572–597.
- Miyamichi, K., Shlomai-Fuchs, Y., Shu, M., Weissbourd, B.C., Luo, L., and Mizrahi, A. (2013). Dissecting local circuits: parvalbumin interneurons underlie broad feedback control of olfactory bulb output. *Neuron* *80*, 1232–1245.
- Mombaerts, P. (2006). Axonal wiring in the mouse olfactory system. *Annu. Rev. Cell Dev. Biol.* *22*, 713–737.
- Mombaerts, P., Wang, F., Dulac, C., Chao, S.K., Nemes, A., Mendelsohn, M., Edmondson, J., and Axel, R. (1996). Visualizing an olfactory sensory map. *Cell* *87*, 675–686.
- Nikolaev, A., Leung, K.-M., Odermatt, B., and Lagnado, L. (2013). Synaptic mechanisms of adaptation and sensitization in the retina. *Nat. Neurosci.* *16*, 934–941.
- Ohmomo, H., Ina, A., Yoshida, S., Shutoh, F., Ueda, S., and Hisano, S. (2009). Postnatal changes in expression of vesicular glutamate transporters in the main olfactory bulb of the rat. *Neuroscience* *160*, 419–426.
- Ohshiro, T., Angelaki, D.E., and DeAngelis, G.C. (2011). A normalization model of multisensory integration. *Nat. Neurosci.* *14*, 775–782.
- Olsen, S.R., and Wilson, R.I. (2008). Lateral presynaptic inhibition mediates gain control in an olfactory circuit. *Nature* *452*, 956–960.
- Olsen, S.R., Bhandawat, V., and Wilson, R.I. (2010). Divisive normalization in olfactory population codes. *Neuron* *66*, 287–299.
- Oyibo, H.K., Znamenskiy, P., Oviedo, H.V., Enquist, L.W., and Zador, A.M. (2014). Long-term Cre-mediated retrograde tagging of neurons using a novel recombinant pseudorabies virus. *Front Neuroanat* *8*, 86.
- Pinching, A.J., and Powell, T.P. (1971). The neuron types of the glomerular layer of the olfactory bulb. *J. Cell Sci.* *9*, 305–345.
- Robinson, B.L., and McAlpine, D. (2009). Gain control mechanisms in the auditory pathway. *Curr. Opin. Neurobiol.* *19*, 402–407.
- Schoppa, N.E., and Westbrook, G.L. (2002). AMPA autoreceptors drive correlated spiking in olfactory bulb glomeruli. *Nat. Neurosci.* *5*, 1194–1202.
- Shepherd, G.M. (1972). Synaptic organization of the mammalian olfactory bulb. *Physiol. Rev.* *52*, 864–917.
- Soucy, E.R., Albeanu, D.F., Fantana, A.L., Murthy, V.N., and Meister, M. (2009). Precision and diversity in an odor map on the olfactory bulb. *Nat. Neurosci.* *12*, 210–220.
- Spors, H., Wachowiak, M., Cohen, L.B., and Friedrich, R.W. (2006). Temporal dynamics and latency patterns of receptor neuron input to the olfactory bulb. *J. Neurosci.* *26*, 1247–1259.
- Spors, H., Albeanu, D.F., Murthy, V.N., Rinberg, D., Uchida, N., Wachowiak, M., and Friedrich, R.W. (2012). Illuminating vertebrate olfactory processing. *J. Neurosci.* *32*, 14102–14108.
- Stopfer, M., Jayaraman, V., and Laurent, G. (2003). Intensity versus identity coding in an olfactory system. *Neuron* *39*, 991–1004.
- Tatti, R., Bhaukaurally, K., Gschwend, O., Seal, R.P., Edwards, R.H., Rodriguez, I., and Carleton, A. (2014). A population of glomerular glutamatergic neurons controls sensory information transfer in the mouse olfactory bulb. *Nat. Commun.* *5*, 3791.
- Vickers, N.J. (2000). Mechanisms of animal navigation in odor plumes. *Biol. Bull.* *198*, 203–212.
- Vinje, W.E., and Gallant, J.L. (2000). Sparse coding and decorrelation in primary visual cortex during natural vision. *Science* *287*, 1273–1276.
- Wachowiak, M., Economo, M.N., Díaz-Quesada, M., Brunert, D., Wesson, D.W., White, J.A., and Rothermel, M. (2013). Optical dissection of odor information processing in vivo using GCaMPs expressed in specified cell types of the olfactory bulb. *J. Neurosci.* *33*, 5285–5300.
- Whitesell, J.D., Sorensen, K.A., Jarvie, B.C., Hentges, S.T., and Schoppa, N.E. (2013). Interglomerular lateral inhibition targeted on external tufted cells in the olfactory bulb. *J. Neurosci.* *33*, 1552–1563.
- Willmore, B., and Tolhurst, D.J. (2001). Characterizing the sparseness of neural codes. *Network* *12*, 255–270.
- Wilson, R.I. (2013). Early olfactory processing in *Drosophila*: mechanisms and principles. *Annu. Rev. Neurosci.* *36*, 217–241.
- Wilson, R.I., and Mainen, Z.F. (2006). Early events in olfactory processing. *Annu. Rev. Neurosci.* *29*, 163–201.
- Yaksi, E., and Wilson, R.I. (2010). Electrical coupling between olfactory glomeruli. *Neuron* *67*, 1034–1047.
- Zhu, P., Frank, T., and Friedrich, R.W. (2013). Equalization of odor representations by a network of electrically coupled inhibitory interneurons. *Nat. Neurosci.* *16*, 1678–1686.
- Zhuang, X., Masson, J., Gingrich, J.A., Rayport, S., and Hen, R. (2005). Targeted gene expression in dopamine and serotonin neurons of the mouse brain. *J. Neurosci. Methods* *143*, 27–32.

**Neuron, Volume 87**

**Supplemental Information**

**An Interglomerular Circuit Gates Glomerular Output and Implements Gain Control in the Mouse**

**Olfactory Bulb**

Arkarup Banerjee, Fred Marbach, Francesca Anselmi, Matthew S. Koh, Martin B. Davis, Pedro Garcia da Silva, Kristen Delevich, Hassana K. Oyibo, Priyanka Gupta, Bo Li, and Dinu F. Albeanu

## **Supplemental materials**

The Supplemental materials contain:

1. Supplemental movies 1-5
2. Supplemental table 1
3. Supplemental notes
4. Supplemental figures S1-S8 with figure captions
5. Supplemental experimental procedures

### **Supplemental movies**

Each movie shows the sequence of images acquired at 5 Hz via widefield imaging of the olfactory bulb (OB) in response to 12 s pulse of odor. Odor presentation was flanked by clean air periods (12 s) both before and after. For visualization purpose, the baseline fluorescence (average of pre odor frames) was subtracted from each frame. The frame rate is sped up 10 times. Specific details for each movie are listed below.

#### **Supplemental movie 1 - related to Figure 1**

Responses from a DAT-Cre mouse crossed to Ai38 (ROSA-LoxP-STOP-LoxP-GCaMP3.0) upon presentation of Isoamyl acetate. Odor was diluted 1:10,000 times in mineral oil.

#### **Supplemental movie 2 - related to Figure 1**

Responses from a DAT-Cre mouse crossed to Ai38 (ROSA-LoxP-STOP-LoxP-GCaMP3.0) upon presentation of Isoamyl acetate. Odor was diluted 1:100 times in mineral oil.

#### **Supplemental movie 3 - related to Figure 1**

Responses from a DAT-Cre mouse crossed to Ai38 (ROSA-LoxP-STOP-LoxP-GCaMP3.0) upon presentation of 2-heptanone. Odor was diluted 1:100 times in mineral oil.

#### **Supplemental movie 4 - related to Figure 1**

Responses from a TH-Cre mouse injected with AAV2.9-DIO-GCaMP3.0 upon presentation of 2-heptanone. Odor was diluted 1:10,000 times in mineral oil.

#### **Supplemental movie 5 - related to Figure 1**

Responses from a TH-Cre mouse injected with AAV2.9-DIO-GCaMP3.0 upon presentation of Heptanal. Odor was diluted 1:100 times in mineral oil.

#### **Supplemental Table 1: Odor Lists - related to Figure 1, 2, and 7.**

## Supplemental notes – related to Figure 1 and Figure 6

### Control experiments concerning the spatial extent of the widefield odor signals.

We wanted to verify that the large spatial extent of the diffuse signals was not due to light scattering. To do so, we imaged OMP-SpH mice (Bozza et al., 2004), which express a fluorescent reporter of presynaptic release (synapto-pHluorin, SpH) in OSN terminals. SpH responses were spatially localized with sharp boundaries as indicated by single-pixel correlation analysis (**Figure 1I** and **S2C-F**) in contrast to the widespread GCaMP3.0 signals in DAT+ cells throughout the bulb surface (**Figure S2G-I**).

A recent study that monitored SA cell responses by targeting GCaMP3.0 expression to TH+ neurons reported only focal responses (Wachowiak et al., 2013). In contrast, we also observed widespread odor responses in TH-Cre mice (**Figure S2J-L, Supplemental movies 4-5**). Given the smaller amplitude of the diffuse component as compared to the focal component of the odor responses, differences in threshold criteria for signal detection and/or in the optical configuration may explain the observed difference.

We hypothesized that the widespread response results from activation of the long-range processes of DAT+ cells associated with only a few odor-activated glomeruli. To confirm this hypothesis, we focally expressed GCaMP3.0 in DAT+ cells and imaged neuropil responses in regions distal to the injection site (>1 mm away), where no labeled cell bodies were found (**Figure S1A** and **S3A-B**). Two-photon imaging of neuropil revealed sparse and odor-specific responses similar to DAT+ cell bodies (**Figure S3B-C** and **2B-E**). In contrast, wide-field imaging of GCaMP3.0 signals in the same OB showed focal activity patterns exclusively near the injection site and diffuse signals as far as 1 mm away. We conclude that calcium responses from DAT+ cell neuropil underlie the diffuse component of the widefield signal (**Figure S3D**).

### In-vitro whole cell recordings to probe synaptic and electrical connections between DAT+ and M/T cells.

*In-vivo* pharmacological experiments suggested the possibility of electrical coupling between DAT+ and M/T cells (**Figure 5**), with the caveat that the synaptic block was not complete (**Figure S6D**). Therefore, to investigate the interaction between DAT+ cells and M/T cells under controlled experimental conditions, we performed whole cell recordings from mitral cells in acute bulb slices from DAT-Cre mice injected with AAV2.9-DIO-ChR2-EYFP or crossed to Ai32 mice. We confirmed in wild-type mice that light stimulation intensities used in all subsequent experiments did not evoke any significant current in recorded mitral cells or ET cells *in vitro* (**Figure S7C-E**). Full-field stimulation of ChR2-expressing DAT+ cells did not produce an outward current in M/T cells in voltage clamp, but reduced the number of EPSCs in current clamp (**Figure S8A-C**), resulting in an apparent outward current when averaged across trials (**Figure S8C**). The absence of direct synaptic inhibition onto M/T cells is consistent with a recent study (Whitesell et al., 2013). We also did not observe any light-induced inward currents

after the application of synaptic blockers (**Figure S8C-ii**). These results argue against a direct synaptic or electrical connection between DAT+ cells and M/T cells.

Figure S1: related to Figure 1

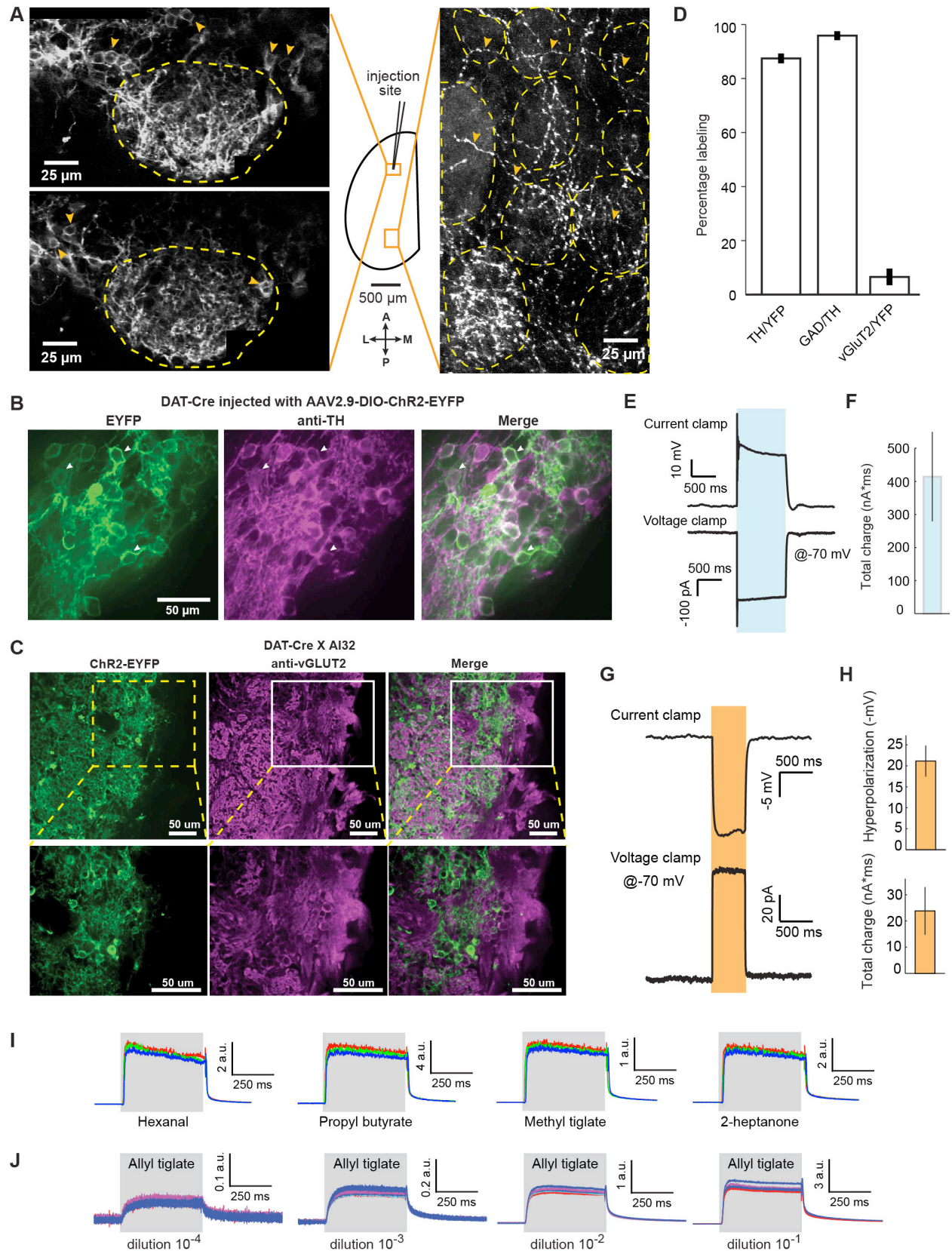


**Figure S1: Histochemical, anatomical and optogenetic characterization of DAT+ cells.**

- A)** *In vivo* two-photon projection images of fields of view (FOVs) imaged close and far away from the AAV2.9-DIO-ChR2-EYFP virus injection site. Dashed lines mark outlines of visually identified glomeruli throughout the z-stack. Fiduciary marks indicate a few example DAT+ cell bodies.
- B)** Confocal images of sagittal bulb slices from a DAT-Cre mouse injected with AAV2.9-DIO-ChR2-EYFP showing ChR2-EYFP fluorescence (*left*) and immunolabeling with a TH antibody (*center*). *Right*, Pseudo-colored merge of EYFP (green) and anti-TH (magenta) staining showing co-expression of TH in targeted neurons. Fiduciary marks show individual cell bodies.
- C)** Confocal images of sagittal bulb slices from a DAT-Cre X Ai32 mouse showing ChR2-EYFP fluorescence (*left*) and immunolabeling with anti vGLUT2 antibody (*center*). *Right*, Pseudo-colored merge of EYFP (green) and anti-vGLUT2 (magenta) staining showing insignificant co-expression.
- D)** Percentage of co-labeled cells in various dual and triple immunolabeling experiments. Numbers indicate mean  $\pm$  SEM (total cell count TH/YFP: n = 226, GAD/TH: n = 118, vGlut2/YFP: n = 115).
- E)** Example current clamp (*top*) and voltage clamp (*bottom*) traces (average of 10 repeats) from a ChR2-EYFP expressing DAT+ cell upon 1 s of blue light stimulation.
- F)** Summary of total light-induced charge for 6 ChR2-EYFP expressing DAT+ cells.
- G)** Example current clamp (*top*) and voltage clamp (*bottom*) traces (average of 10 repeats) from a NpHR3.0-EYFP expressing DAT+ cell upon 0.5 s of red light stimulation.
- H)** Average hyperpolarization (*top*, across 9 cells) and total charge (*bottom*, across 7 cells) induced in DAT+ cells expressing NpHR3.0-EYFP.
- I)** PID traces for interleaved presentations of 4 odors (3 repeats). Colors indicate individual trials. All odors at  $10^{-2}$  dilution in mineral oil. PID output is represented in arbitrary units (a.u.).
- J)** PID traces for increasing concentrations of a representative odor - Allyl tiglate. Odor concentrations are reported as nominal dilutions in mineral oil. Colors indicate individual trials (5 repeats). PID output is represented in arbitrary units (a.u.).

**Figure S2: related to Figure 1 and Figure 2**

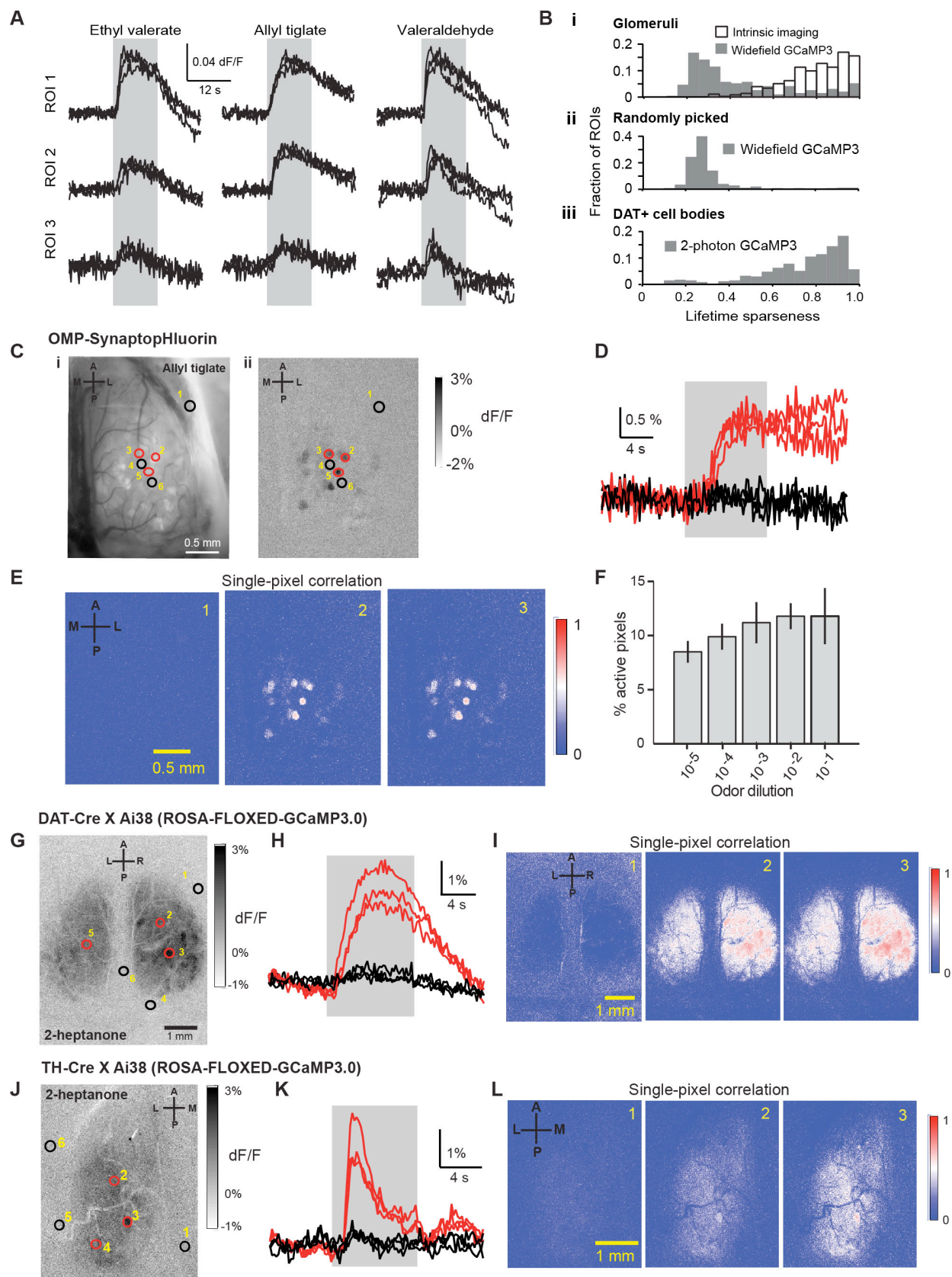


**Figure S2: Characterization of widefield odor responses of DAT+ cells.**

**A)** Baseline-subtracted, normalized widefield GCaMP3.0 signals (dF/F) from 3 glomerular ROIs on the bulb surface in response to Ethyl valerate, Allyl tiglate and Valeraldehyde. All odors at  $10^{-2}$  nominal dilution in mineral oil. Black traces indicate individual trials. Gray band indicates odor presentation.

**B)** Distributions of lifetime sparseness of ROIs chosen by IOI, widefield and two-photon GCaMP3.0 odor responses of DAT+ cells. *(i)* Lifetime sparseness of intrinsic optical imaging (IOI) (empty black bars, 347 ROIs, 5 bulbs) and widefield GCaMP3.0 responses (gray bars, 188 ROIs, 3 bulbs, 3 mice) of all glomerular ROIs. Glomerular ROIs were chosen using glomerular outlines obtained from IOI. Numbers indicate mean  $\pm$  SEM. *(ii)* Lifetime sparseness of GCaMP3.0 responses of randomly chosen glomerular size ROIs (gray bars, 347 ROIs, 5 bulbs, 3 mice). *(iii)* Lifetime sparseness of two-photon GCaMP3.0 responses of DAT+ cell bodies (gray bars, 331 ROIs, 4 mice).

**C)** Widefield image showing resting (*left*) and odor-evoked (dF/F image, *right*, Allyl tiglate,  $10^{-1}$  dilution) fluorescence in the exposed olfactory bulb of an OMP-SpH (+/-) mouse. Open circles indicate six randomly chosen glomerular size ROIs on the exposed bulb surface. Red circles correspond to ROIs drawn over responsive glomeruli. Black circles correspond to ROIs drawn over non-responsive glomeruli, or bone. Numbers indicate ROI index.

**D)** Average responses of ROIs shown in **C**, upon presentation of Allyl tiglate ( $10^{-1}$  dilution). Each trace represents the average change in fluorescence (3 repeats) with respect to pre-odor baseline. Colors indicate ROIs selected on bulb surface (red) and bone (black) respectively.

**E)** Color maps showing correlation of the average odor-evoked response of each pixel with a given reference pixel chosen from the first three ROIs shown in **C**. ROI index of the glomerular ROI used to choose the reference pixel is indicated in the top right corner of each color map.

**F)** Average spatial spread of SpH responses as a function of increasing odor concentration. Each bar shows average for all bulb-odor pairs (dilutions  $10^{-5}$  to  $10^{-1}$ : 2 bulbs, 7 odors). Error bars indicate SEM. Odor concentrations are reported as nominal odor dilutions in mineral oil.

**G)** Widefield image showing odor-evoked (dF/F image, 2-heptanone,  $10^{-2}$  dilution) GCaMP3.0 fluorescence in the exposed olfactory bulb of DAT-Cre x Ai38 reporter mouse line. Open circles indicate six randomly chosen glomerular size ROIs on the exposed bulb surface (red) and bone (black). Numbers indicate ROI index.

**H)** Average response of the ROIs shown in **G**, in response to 2-heptanone ( $10^{-2}$  dilution). Each trace represents the average change in fluorescence (3 repeats) with respect to pre-odor baseline. Colors indicate ROIs selected on bulb surface (red) and bone (black) respectively.

**I)** Color maps showing correlation of the average odor-evoked response of each pixel with a randomly chosen reference pixel from each of the first three glomerular ROI shown in **G**. ROI index of the glomerular ROI used to choose the reference pixel is indicated in the top right corner of each color map.

**J)** Odor-evoked GCaMP3.0 fluorescence in an example hemi-bulb from a TH-Cre mouse injected with DIO-GCaMP3-AAV2.9 in response to 2-heptanone ( $10^{-2}$  dilution). Open circles indicate six randomly chosen glomerular size ROIs on the exposed bulb surface (red) and bone (black). Numbers indicate ROI index.

**K)** Average response of ROIs shown in **J**. Each trace represents the average change in fluorescence (3 repeats) with respect to pre-odor baseline. Colors indicate ROIs selected on bulb surface (red) and bone (black) respectively.

**L)** Color maps showing correlation of the average odor-evoked response of each pixel with a given reference pixel chosen from the first three glomerular ROI shown in **J**. ROI index of the glomerular ROI used to choose the reference pixel is indicated in the top right corner of each color map.

**Figure S3: related to Figure 2**

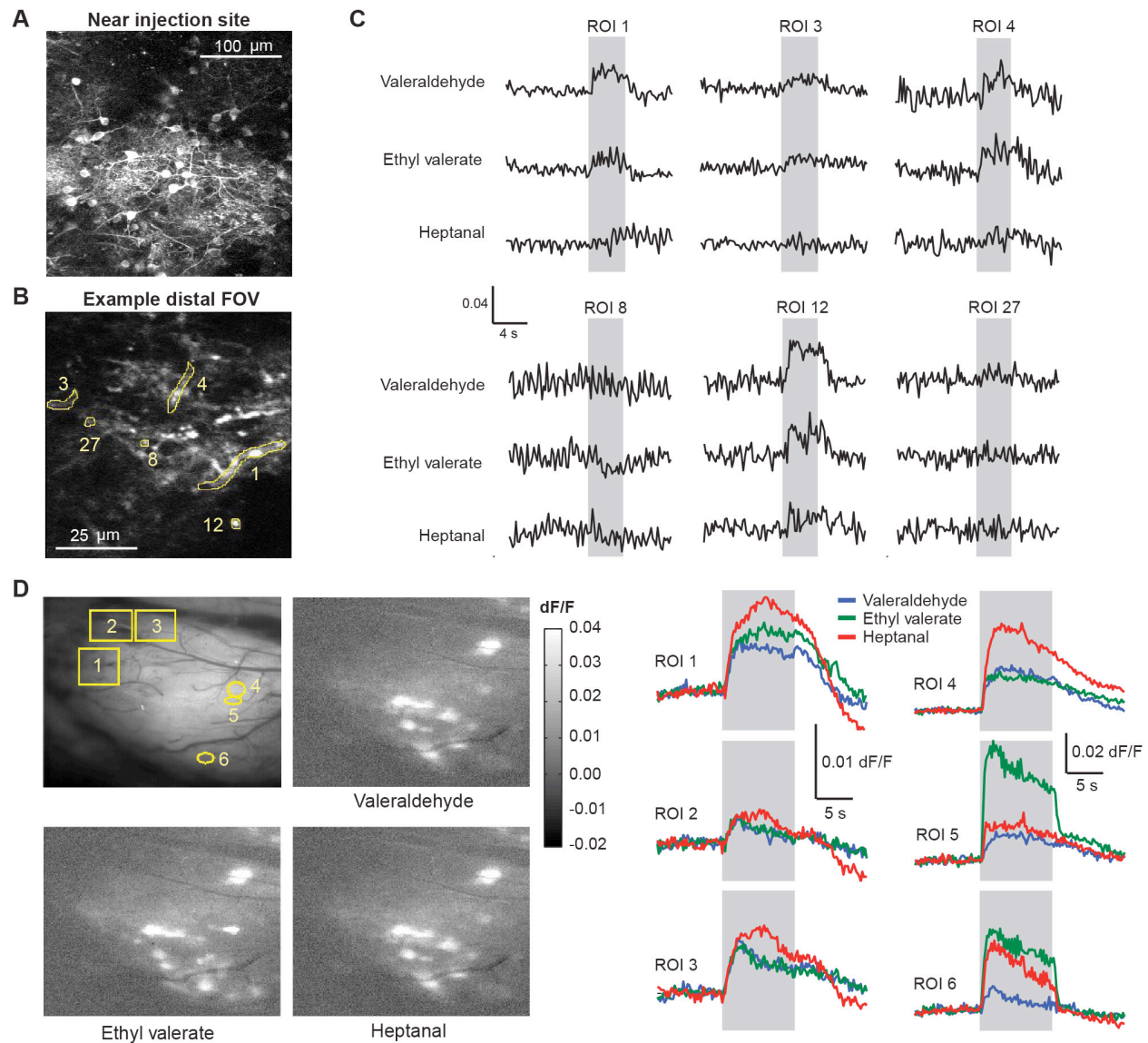


**Figure S3: Two-photon and widefield odor signals from DAT+ cell neuropil.**

**A)** Maximum projection image of a z-stack proximal to the focal injection site showing dense labeling of DAT+ cell bodies.

**B)** Image of an example field-of-view (FOV) far from the injection site (> 1.5 mm) averaged over 100 frames at 5 Hz. Six regions of interest (ROIs) were chosen on the neuropil of DAT+ cells, including a few boutons. No DAT+ cell bodies were observed this far from the injection site.

**C)** Average baseline subtracted normalized responses (dF/F) of six representative neuropil ROIs (as indicated on **B**) to three odors - Valeraldehyde, Ethyl Valerate and Heptanal.

**D)** Widefield GCaMP3 odor signals (dF/F) from three ROIs (4, 5 and 6) selected near the injection site and three ROIs (1, 2 and 3) selected far from the injection site. Distinct glomeruli were activated near the injection site for the three odors - Valeraldehyde, Ethyl valerate and Heptanal. No activated glomeruli were seen in the anterior aspects of the same OB as above, far from the injection site. However, the three ROIs (1, 2 and 3) far from the injection site showed robust GCaMP3 signals to all the three odors.

**Figure S4: related to Figure 3**

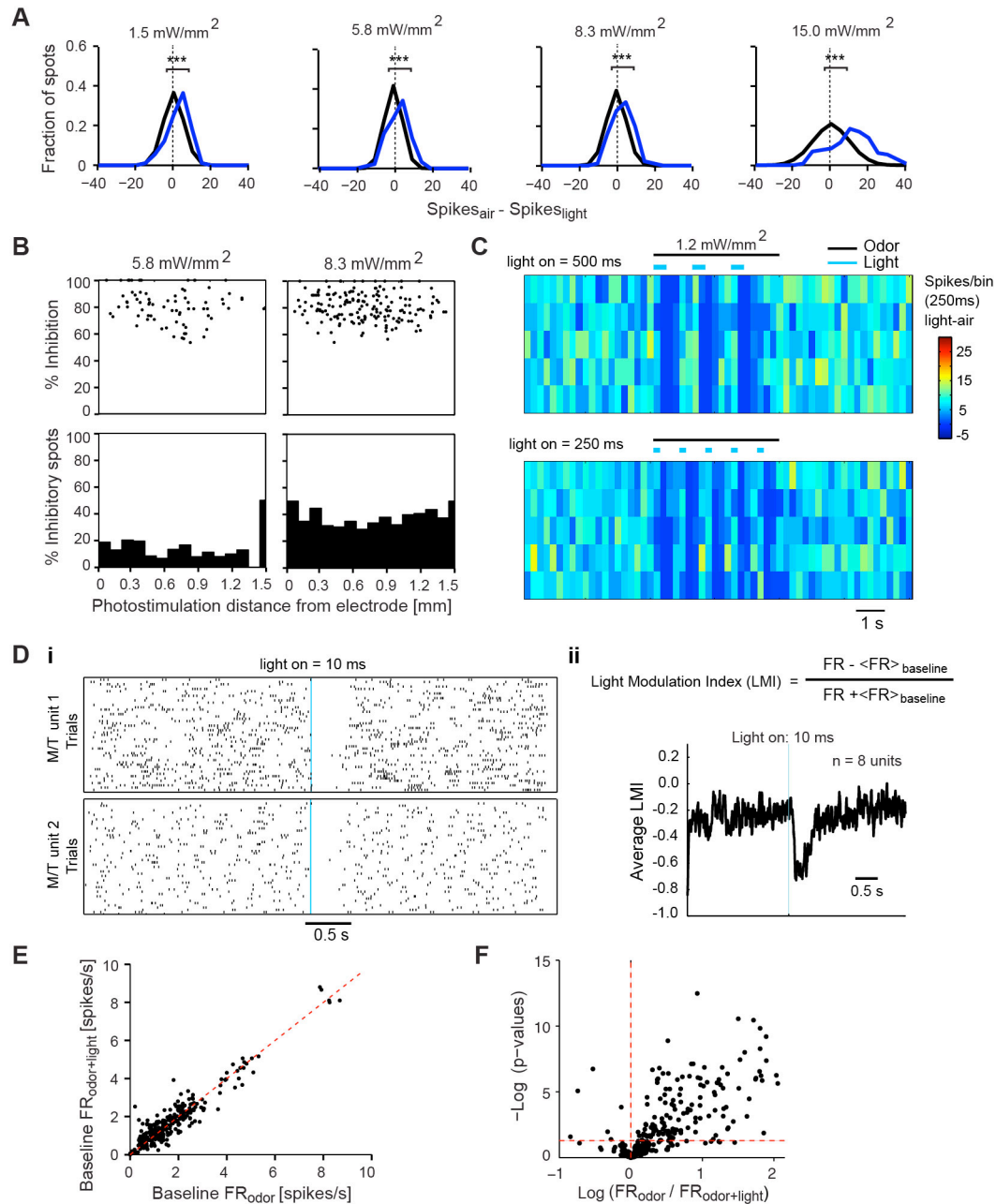


**Figure S4: Effects of photoactivating DAT+ cells on M/T cell firing.**

**A**) Distribution of difference in spike counts ( $\Delta$  spikes) of the recorded M/T unit (shown in **Figure 3B**), upon photostimulation of individual light spots, compared to pre-stimulation period at various light intensities (1.5, 5.8, 8.3, 15 mW/mm<sup>2</sup>). Blue line shows the experimentally observed distribution. Black line shows distribution of differences between independent sets of randomly shuffled pre-stimulation periods. At all light intensities, the experimentally obtained distribution was significantly right-shifted compared to the shuffled control, indicating light-induced inhibition. Paired t-test, \*\*\* denote  $p < 0.001$ .

**B)** *Top*, Strength of light-evoked inhibition as a function of photostimulation distance from the recording site for all M/T units at two light intensities (5.8 mW/mm<sup>2</sup> n = 5, 8.3 mW/mm<sup>2</sup> n = 4). Each dot represents evoked-inhibition upon stimulation of an individual spot. Only spots that evoked a significant change from baseline are plotted (two-sample t-test, p < 0.05). *Bottom*, Fraction of significantly inhibited spots as a function of photostimulation distance from the recording site (two-sample t-test, p < 0.05) at two light intensities (5.8, 8.3 mW/mm<sup>2</sup>). Each dot/bar denotes average of all spots from all recorded M/T units at the respective photostimulation distance and light intensity.

**C)** Baseline subtracted PSTH of an M/T cell upon full-field blue light activation of DAT+ cells for 500 ms (*top*) and 250 ms (*bottom*). The black and blue lines indicate odor and light stimulation respectively.

**D)** *(i)* Raster-plot of two M/T cell units upon full-field blue light activation of DAT+ cells for 10 ms. Each row represents an individual trial. The blue bar denotes the light-on period. *(ii)* Average Light Modulation Index as a measure of light induced suppression of M/T cell spontaneous activity (n = 8 M/T units, 2 mice) for 10 ms light activation of DAT+ cells. Light Modulation Index was calculated as the normalized difference in firing rate (FR) between every 5 ms bin and the average baseline FR. The plot has been smoothed with a 5 ms sliding window. The blue bar denotes the light-on period.

**E)** Scatter plot of average baseline firing rates of individual M/T units preceding the 'odor' and 'odor + light' conditions. Diagonal unity line marks slope of 1, indicating no change in firing rate; 351 pairs, 41 M/T units from 6 mice.

**F)** Volcano plot of light-induced change in odor-evoked firing of individual M/T units (FR odor / FR odor+light) and p-values obtained from a two-sample t-test. All values are plotted on log scale. Solid red line indicates p-value cutoff for significant change in firing (p < 0.05). Quadrants *left* and *right* of the dotted red line indicate light-induced excitation and inhibition respectively.

**Figure S5: related to Figure 4**

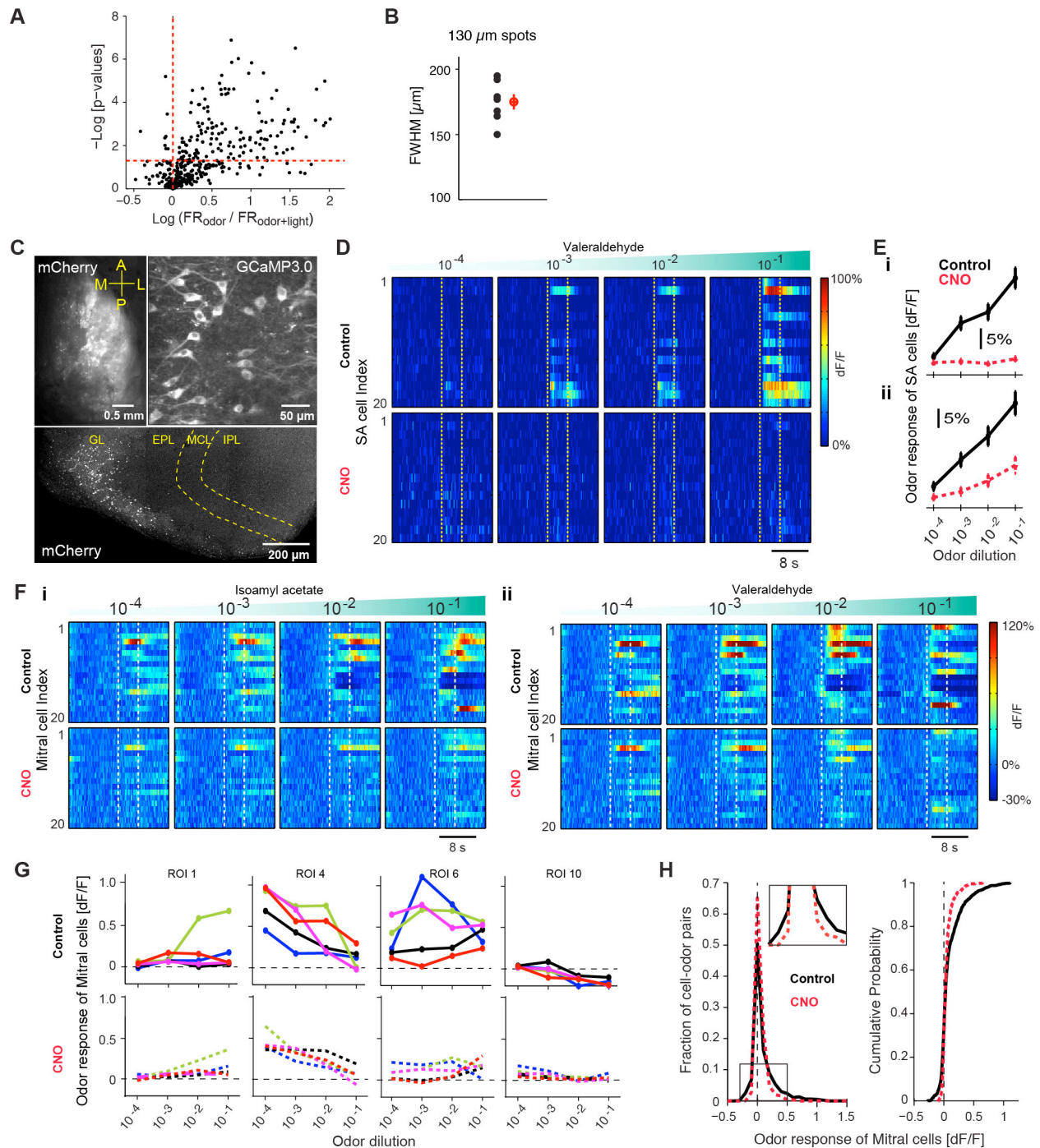


**Figure S5: Optogenetic and pharmacogenetic silencing of DAT+ cells suppresses M/T odor responses.**

**A**) Effect of silencing NpHR3.0 expressing DAT+ cells. Volcano plot of light-induced change in odor-evoked firing of individual M/T units ( $\text{FR}_{\text{odor}} / \text{FR}_{\text{odor+light}}$ ) and p-values obtained from a two-sample t-test. All values are plotted on a log scale. Horizontal red line indicates p-value cutoff for significant change in firing ( $p < 0.05$ ). Quadrants *left* and *right* of the vertical red line indicate light-induced excitation and inhibition respectively.

**B)** Summary of estimated full-width-at-half-maxima (FWHM) of ‘cold-spots’ obtained (see **Figure 4D**) by fitting a normalized Gaussian distribution across 7 M/T units from 2 mice. Error bar denotes standard error of the mean.  $FWHM = 175 \pm 5.9 \mu m$ ,  $n = 7$  cells.

**C)** Images from the olfactory bulb of a DAT-Cre x Ai38 mouse injected with AAV2.9-DIO-DREADDi-mCherry virus in the glomerular layer, and with PRV-Cre in the piriform cortex. *Top, Left*: widefield image showing mCherry expression in the exposed olfactory bulb; *Top, Right*: *In vivo* two-photon image of resting fluorescence showing GCaMP3.0 expression in M/T cells. *Bottom*, confocal image showing selective expression of mCherry only in the glomerular layer.

**D)** Baseline-subtracted, normalized GCaMP3.0 signals from an example imaging session of DAT+ cell responses to increasing concentrations of heptanal before (control, *Top*) and after CNO injection (*Bottom*). Stimulus concentrations are reported as nominal dilution in mineral oil. Each row represents an individual DAT+ cell (ROI) in the same field of view. Color indicates normalized change in fluorescence with respect to pre-odor baseline (dF/F). Dotted lines indicate odor presentation (4 s). Images were acquired at 5 Hz.

**E)** (i) Average odor-evoked response (dF/F) of all DAT+ cells (20 ROIs) shown in **D**, across five odors as a function of increasing odor concentration. Black and red (dotted) lines show responses before and after CNO injection. Error bars indicate standard error of mean. (ii) Average odor-evoked response (dF/F) of all responsive DAT+ cells (110 cells, 3 mice), across five odors as a function of increasing odor concentration. Black and red (dotted) lines show responses before and after CNO addition. Error bars indicate SEM.

**F)** Baseline-subtracted, normalized GCaMP3.0 signals from an example imaging session of M/T cells to increasing concentrations of Isoamyl acetate (i) and Valeraldehyde (ii) before (control, *Top*) and after (CNO, *Bottom*) CNO injection. Stimulus concentrations are reported as nominal dilution in mineral oil. Each row represents an individual M/T cell (ROI). Color indicates relative change in fluorescence with respect to pre-odor baseline (dF/F). Dotted lines indicate odor presentation. Images were acquired at a frame rate of 5 Hz.

**G)** Average odor-evoked response (dF/F, 2-3 repeats) of four example M/T cells (ROIs) shown in **F**, to five odors, as a function of increasing odor concentration, before (control, solid lines, *Top*) and after (CNO, dotted lines, *Bottom*) CNO injection. Colors indicate individual odors (same as **Figure 2G**).

**H)** Summary histogram (*Left*) and cumulative distribution (*Right*) of M/T odor responses as a function of normalized response strength (dF/F) before (black) and after (red) CNO injection. 49 cells, 842 cell-odor pairs, 3 mice.

**Figure S6: related to Figure 5**

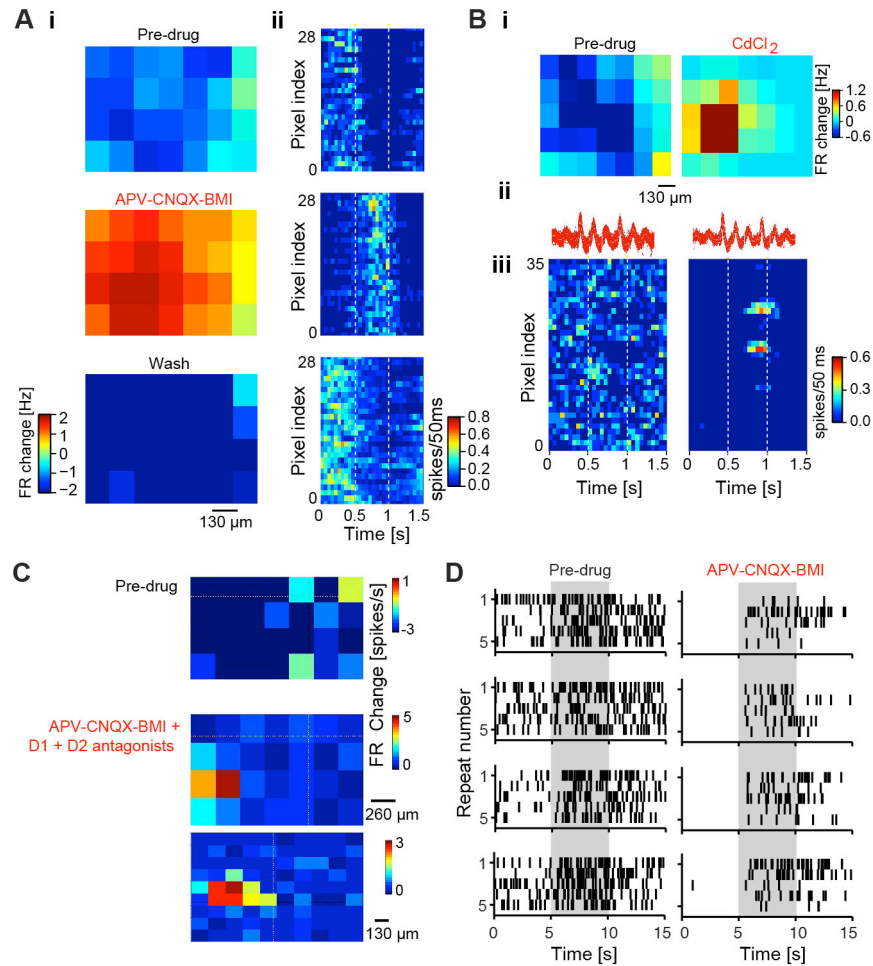


**Figure S6: Light-induced suppression of M/T cells by DAT+ cells switches to excitation in presence of synaptic blockers.**

**A)** (i) 2D light map from a DAT-cre mouse injected with AAV2.9-DIO-ChR2-EYFP virus, showing change in firing of an example M/T unit upon random mapping of the bulb surface with blue light spots ( $130 \mu\text{m} \times 130 \mu\text{m}$ ,  $15 \text{ mW/mm}^2$ ) before (*top*), during blocking synaptic transmission via APV-CNQX-BMI (*middle*) and post-wash (*bottom*) of the drug cocktail. Color indicates average firing rate (FR) change in M/T spiking with respect to pre-light stimulation baseline. (ii) PSTH of all spots from the same light mapping session in (i), before (*top*), during (*middle*) and post-wash (*bottom*) drug application. Pixels, from *bottom left* to *top right* corner, in the light map are re-ordered as *top to bottom* rows in the PSTH. Dotted lines indicate the photostimulation period. Color indicates firing rate in 50 ms bins.

**B)** (i) 2D light maps from a DAT-cre mouse injected with AAV2.9-DIO-ChR2-EYFP virus before (*left*) and during (*right*) application of CdCl<sub>2</sub>. (ii) Spike waveforms of the M/T unit in (i) before (*left*) and during (*right*) application of CdCl<sub>2</sub>. (iii) PSTH of all spots for an example M/T unit, upon random mapping of the bulb surface with blue light spots ( $130 \mu\text{m} \times 130 \mu\text{m}$ ,  $15 \text{ mW/mm}^2$ ) before (*left*) and during (*right*) CdCl<sub>2</sub>.

**C)** 2D light maps from a DAT-cre mouse injected with DIO-ChR2-EYFP AAV virus before (*Top*) and during (*Middle, Bottom*) application of APV-CNQX-BMI + D1 and D2 receptor antagonists (SKF83566 hydrobromide, sulpiride). *Top and middle* light maps show change in firing rate of an example M/T unit, upon random mapping of the bulb surface with blue light spots ( $260 \mu\text{m} \times 260 \mu\text{m}$ ,  $15 \text{ mW/mm}^2$ ). Bottom light map shows change in firing

rate of the same M/T unit, upon random mapping of the bulb surface with smaller blue light spots ( $130 \mu\text{m} \times 130 \mu\text{m}$ ,  $15 \text{ mW/mm}^2$ , 3 M/T units, 2 mice).

**D**) Raster of an example M/T unit to four odors (from *top to bottom*: Allyl tiglate, Isoamyl acetate, Valeraldehyde, Ethyl valerate; dilution  $10^{-2}$ ) before (*left*) and after (*right*) addition of APV-CNQX-BMI. Each row represents an individual trial. Gray bar indicates duration of odor presentation.

**Figure S7: related to Figure 4**

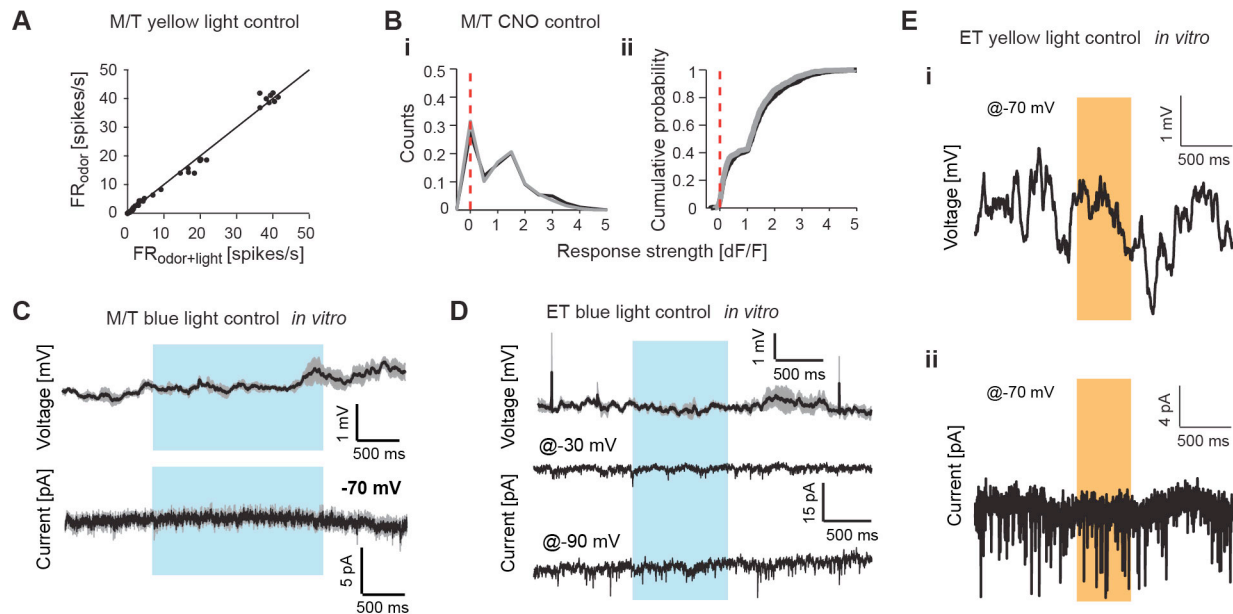


**Figure S7: Optogenetic and pharmacogenetic controls in wild-type mice.**

**A**) Scatter plot of average firing rates of M/T units during ‘odor’ and ‘odor+light’ conditions in wild-type mice upon full-field yellow light stimulation ( $3 \text{ mW/mm}^2$ ). Diagonal marks slope of 1, indicating no change in firing rate (5 M/T units, 35 cell-odor pairs, 3 mice).

**B**) Histogram (*i*) and cumulative distribution (*ii*) of M/T GCaMP3.0 odor responses as a function of normalized response strength (dF/F) before (black) and after (gray) CNO injection (51 M/T cells, 1020 cell-odor pairs, 3 mice).

**C**) Average current clamp (*top*) and voltage clamp (*bottom*) traces recorded from M/T cells in bulb slices of wild-type mice, upon blue light stimulation ( $7 \text{ mW}$ , at the objective exit). Black line and shaded region represent mean and SEM (3 cells).

**D**) Average current clamp (*top*) and voltage clamp (*middle, bottom*) traces recorded from ET cells in bulb slices of wt mice, upon blue light stimulation ( $7 \text{ mW}$ , at the objective exit). Black line and shaded region represent mean and SEM (3 cells in current clamp, 2 cells in voltage clamp).

**E**) Current clamp (*i*) and voltage clamp (*ii*) (holding potential of  $-70 \text{ mV}$ ) traces recorded from an ET cell in bulb slices of wt mice, upon red light stimulation ( $0.8 \text{ mW/mm}^2$ ).

**Figure S8: related to Figure 6**

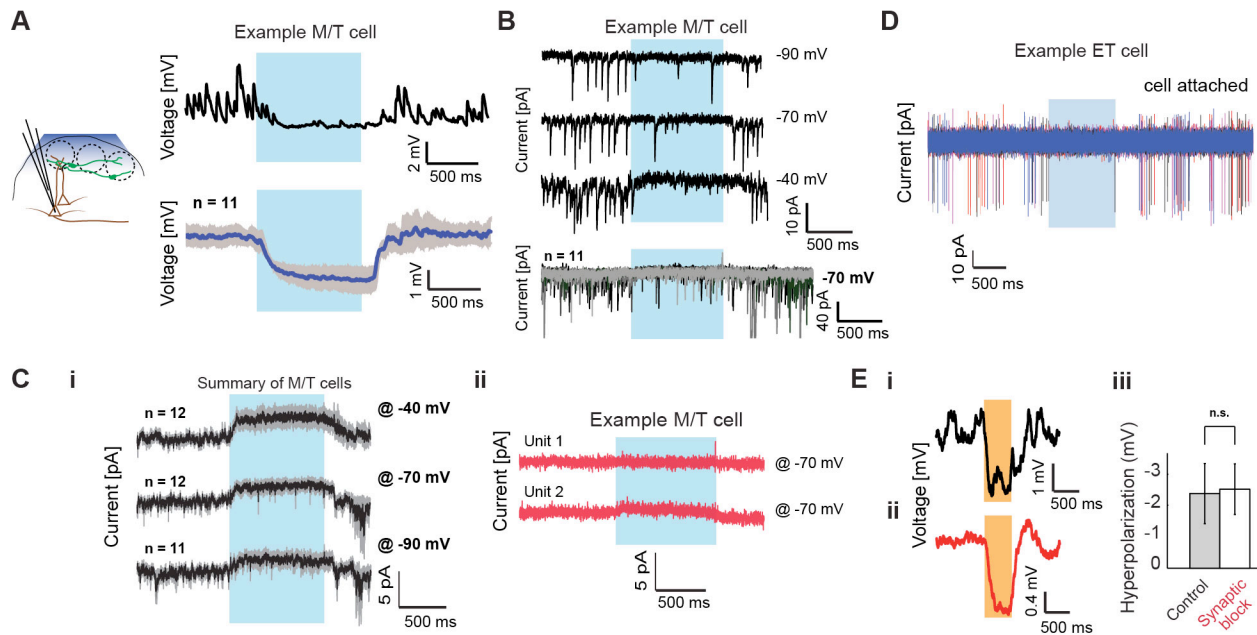


**Figure S8: Whole-cell recordings from Mitral cells and ET cells during optogenetic manipulations of DAT+ cells**

**A)** *Left:* Schematic of the experiment. *Top, Right:* Light-induced hyperpolarization in an example current clamp trace from a M/T cell upon full-field blue light stimulation (1 s) of ChR2-expressing DAT+ cells in an acute horizontal olfactory bulb slice. Black trace shows an individual trial. Blue bar marks duration of light stimulation. *Bottom, Right:* Mean light-induced hyperpolarization across 10 M/T cells upon optogenetic activation (1 s) of DAT+ cells (blue trace). Shaded gray region shows SEM.

**B)** *Top,* Example voltage clamp traces showing light-induced reduction of EPSCs frequency in the example M/T cell shown in **A** upon ChR2 stimulation (1 s) of DAT+ cells at three different holding potentials. Black traces show individual trials. Blue bar marks the duration of light stimulation. *Bottom,* Individual voltage-clamp traces from 11 M/T cells recorded at -70 mV holding potential. Blue bar marks duration of light stimulation.

**C)** *(i)* Average light-induced current trace from mitral cells at three different holding potentials (-40 mV, -70 mV: n = 12 cells; -90 mV: n = 11 cells). Gray shaded region represent the SEM. Blue bar marks duration of light stimulation. *(ii)* Average light-induced current trace from two mitral cells at -70 mV holding potential (10 repeats) in the presence of synaptic blockers (NBQX, APV, picrotoxin, S(-)-eticlopride hydrochloride and SKF83566).

**D)** Superposition of 10 voltage clamp traces from an example ET cell recorded in the cell-attached configuration, showing suppression of spontaneous firing upon blue light stimulation. Colors indicate individual trials.

**E)** Light-induced voltage trace (average of 10 trials) from an example ET cell in control conditions *(i)* or in the presence of synaptic blockers *(ii)*. Summary of average hyperpolarization induced in ET cells upon inactivation of NpHR3.0 expressing DAT+ cells before (n = 8 ET cells) or after synaptic blockers (n = 5 ET cells). They are not significantly different (p-value = 0.93, two-sample t-test).

## **Supplemental Experimental Procedures**

### **Surgical Procedures**

Adult mice (males and females >30 days old, 25-40 g) were anesthetized with ketamine/xylazine (KX, initial dose 70/7 mg/kg), further supplemented via a peristaltic pump (Harvard Apparatus, Pump 11 Plus) and maintained between 40-70 mg/kg throughout the experiment. Temperature was maintained at 37° C using a heating pad (FST TR-200, Fine Science Tools, USA). Respiratory rate and lack of pain reflexes were monitored throughout the experiment. Mice were head-fixed to a thin metal plate with acrylic glue. The skull was thinned using a high-speed dental drill (Foredom, Bethel, CT) and removed completely to reveal the dorsal surface of both bulb hemispheres. For electrophysiological recordings, the dura was removed using a pair of fine forceps. The craniotomy was filled with a thin layer of low melting point agarose (~1.2-1.5%). Cortex buffer was perfused continuously using a perfusion pump (ColePalmer Masterflex C/L). For imaging experiments, a glass cover slide was placed atop to prevent drying and to reduce motion artifacts. All animal procedures conformed to NIH guidelines and were approved by Cold Spring Harbor Laboratory Animal Care and Use Committee.

### **Transgenic mice**

Ai9: ROSA:LoxP-STOP-LoxP:tdTomato

Ai32: ROSA:LoxP-STOP-LoxP:ChR2-EYFP

Ai38: ROSA:LoxP-STOP-LoxP:GCaMP3.0

### **Virus injections**

DAT-Cre mice (males and females; >30 days old) were anesthetized as described above before being placed in a stereotactic frame. To express GCaMP3.0, ChR2 or NpHR3.0, AAV2.9-EF1a-DIO-GCaMP3.0 (UNC Vector core;  $4 \times 10^{12}$  viral particles/ml), AAV2.9-EF1a-DIO-ChR2-EYFP (UNC Vector core;  $4 \times 10^{12}$  viral particles/ml) and AAV2.9-EF1a-DIO-NpHR3.0-EYFP (UNC Vector core;  $8 \times 10^{12}$  viral particles/ml) were injected respectively. To express inhibitory DREADD (Designer Receptor Exclusively Activated by Designer Drugs) in DAT+ cells, AAV2.9-CAG-DIO-hM4Di-mCherry (gift from M. Luo, National Institute of Biological Sciences, Beijing; custom made AAV2.9 virus by UNC Viral Core) was injected in DAT-Cre or DAT-Cre X AI38 (ROSA-LoxP-STOP-LoxP-GCaMP3.0) mice. To express Diphtheria Toxin Receptor (DTR) specifically in DAT+ cells, AAV-FLEX-DTR-GFP virus (gift from T. Jessell & E. Azim, Columbia University, New York) was injected in DAT-Cre or DAT-cre X Thy1-GCaMP3.0 mice. Virus was front loaded into 5 $\mu$ l pipettes (VWR international 53432-706) using a 20 ml syringe connected via a rubber tube. Virus was injected at roughly 30 nl/min by applying pressure using the syringe while visually monitoring the fluid in the pipette. To achieve uniform expression, injections were done at 3 sites per olfactory hemi-bulb at depths of 300/200/100 $\mu$ m from the bulb surface. ~300nl of the respective viruses were injected at each site. Injection

protocol was standardized by post-hoc imaging of expression patterns in injected brains. For slice recordings of horizontal sections, expression of ChR2 was targeted to the glomeruli at the midline. AAV2.9-EF1a-DIO-ChR2-EYFP was injected in two antero-posterior sites located 0.5mm lateral from the midline, each at four depths (1750/1250/750/250 $\mu$ m), ~180 nl per depth. For sparse and localized expression, ~90 nl of AAV2.9-EF1a-DIO-ChR2-EYFP or AAV2.9-EF1a-DIO-GCaMP3.0 was injected only at one anterior or posterior site per hemi-bulb. Mice were allowed to recover for at least two weeks prior to experiments with due animal care.

### **Immuno-histochemistry**

Mice were intra-cardially perfused with 4% Para-Formaldehyde (PFA) immediately after a lethal dose of KX cocktail anesthesia. Brains were stored overnight in 4% PFA. After a few rinses with Phosphate Buffer Saline (PBS), 50  $\mu$ m thick sagittal sections were cut, incubated with 1% H<sub>2</sub>O<sub>2</sub> for 30 minutes and subsequently washed three times with 0.1M TRIS buffer. Slices were transferred to blocking solution (10% goat serum in 0.1 M Tris buffer with 0.1% Triton-100) for 1 hour. The blocking solution was removed and washed with 0.1M TRIS buffer three times before the primary antibody was added for 48 hours at 4° C. The primary antibody was pipetted out and slices were washed 6 times with 0.1M TRIS buffer. The secondary antibody was then added for 4 hours at 4° C. Following 6 washes in PBS, the slices were mounted with Vectashield. Images were acquired using Perkin-Elmer Spinning Disk confocal microscope and were analyzed using Volocity (Perkin-Elmer) and ImageJ (NIH, USA).

Specific primary antibodies used:

1. Tyrosine Hydroxylase (TH): Rabbit anti-Tyrosine Hydroxylase (TH) antibody (Sigma, SAB4300675; diluted 1:1,000 in 0.1M TRIS buffer).
2. Glutamate decarboxylase-67 (GAD67): Mouse anti-Glutamate decarboxylase 67 (GAD67) antibody (Millipore, MAB5406; diluted 1:1000 in 0.1M TRIS buffer).
3. Vesicular Glutamate Transporter-2 (vGluT2): Mouse anti-vesicular glutamate transporter-2 antibody (Millipore, MAB5504; diluted 1:1000 in 0.1M TRIS buffer).

Specific secondary antibodies used:

1. Goat anti-rabbit Alexa 594 (Life technologies, A11037; diluted 1:500 in 0.1M TRIS buffer).
2. Goat anti-mouse Alexa Fluor 647 (Life Technologies, A21235; diluted 1:500 in 0.1M TRIS buffer)

For dual immunolabeling experiments, rabbit anti-TH antibody and rabbit anti-GAD67 antibody were simultaneously added. Secondary antibodies for anti-TH and anti-GAD67 were conjugated to Alexa 594 and Alexa 647 respectively. 3-color images were acquired simultaneously in a spinning disk confocal microscope (Perkin Elmer).

## **Odor delivery**

Odors were delivered using a custom-made odor machine (Dhawale et al., 2010), at a net output flow rate of 1L/min. To maintain constant flow rate, a flow-rate matched clean air stream was used in absence of odor stimulation. For large odor panels, up to 100 odors were used. Odors were diluted at 1:100 ( $10^{-2}$ ) in mineral oil. For concentration series experiments under widefield (**Figure 1**), a dedicated odor machine was used with up to 6 different (1:10-1:10<sup>6</sup>) concentrations per odor. For the two-photon imaging experiments described in **Figure 2F-I**, **7** and **S5**, a subset of five odors (Allyl tiglate, Isoamyl acetate, Valeraldehyde, Ethyl Valerate and Heptanal) were used at four concentrations (1:10-1:10<sup>4</sup>). Odor output was characterized using a photo-ionization device (**Figure S1I-J**, Aurora Scientific). These nominal dilutions do not correspond to absolute odor concentrations. Comparison with PID measurements of saturated odor vapor indicated that the actual concentrations spanned from 0.05 % to 1.3% for the large odor panel and up to 3% for the dilution series odors.

## **Widefield fluorescence and intrinsic optical imaging (IOI)**

LED arrays were used to shine blue light (~470 nm, Luxeon V Lumileds) for GCaMP3.0 imaging, or far red light (~780 nm, Roithner Laser Technik) for intrinsic optical imaging (IOI) on the bulb surface. Images of the OB were acquired with a Vosskuhler 1300-QF CCD camera, coupled to two SLR lenses positioned front to front (Nikkor 105 mm FL, f/2.0 and either Nikkor 50 mm FL, f/1.4, or Voigtlander 35 mm FL, f/1.2) with a pixel size of 12.6  $\mu\text{m}$  or of 8.7  $\mu\text{m}$ , as previously described in detail (Dhawale et al., 2010). For a subset of experiments, GCaMP3.0 imaging and IOI were performed in the same animal. Fluorescence imaging and IOI were alternated across blocks of 20 odors for large odor panel experiments and across individual concentration sets. Blue light intensity was calibrated to avoid photobleaching. IOI and GCaMP3.0 signals were acquired at 25 Hz and 4 Hz respectively. Each trial consisted of 12 s of odor delivery flanked by 12 s of air on both sides. The inter-trial interval was 30 s. Each stimulus was repeated on an average 3 times. Image acquisition was controlled by custom-written software in Labview (National Instruments).

## **Two-photon imaging**

A Chameleon Ultra II Ti:Sapphire femtosecond pulsed laser (Coherent) was used together with a custom built two photon microscope. The shortest optical path was used to bring the laser onto a galvanometric mirrors scanning system (6215HB, Cambridge Technologies). The scanning system projected the incident laser beam tuned at 930 nm through a scan lens (50 mm FL) and tube lens (300 mm FL) to backfill the aperture of an Olympus 20X, 1.0 NA objective. A Hamamatsu modified H7422-40 photomultiplier tube was used as photo-detector and a Pockels cell (350-80 BK and 302RM driver, ConOptics) as beam power modulator. The current output of the PMT was transformed to voltage, amplified (SR570, Stanford Instruments) and digitized using a data acquisition board that also controlled the scanning (PCI 6115, National

Instruments). Image acquisition and scanning were controlled by custom-written software in Labview (National Instruments).

*DAT+ cell imaging:* In a typical experiment, multiple fields of view of  $\sim 300 \times 300 \mu\text{m}$  were sampled in the glomerular layer. Before odor delivery, a z-stack was taken for each field of view (FOV) across the glomerular layer. Glomerular outlines were visually identified from the z-stacks for assignment of DAT+ cell bodies to respective glomeruli. Once an optical plane was chosen, odors were delivered and a time sequence of 120 frames at 4 Hz (10 s air, 8 s odor, 12 s air) was acquired. The inter-trial interval was 30 s. Each odor was typically delivered 2-4 times. For the concentration series experiments, once an optical plane was chosen, a set of five odors at four concentrations ( $1:10$ - $1:10^4$ ) were delivered and time lapse data acquired for 100 frames at 5 Hz (10 s of air, 4 s of odor followed by 6 s of air). The inter-trial interval was 40 s and each stimulus was repeated 2-5 times.

### **Difference between TH-Cre and DAT-Cre mice.**

The reported expression pattern of TH-Cre mice (Wachowiak et al., 2013) shows expression in the glomerular layer, but also in the deeper layers. In contrast, expression in DAT-Cre mice that is restricted to the glomerular layer (**Figure 1A**) and shows considerable overlap for TH antibody (**Figure 1B**). To minimize non-specific targeting of cells other than the glomerular DAT+ cells, we relied on DAT-Cre mice for most experiments reported here. Only in one subset of experiments, we monitored odor responses in TH-Cre mice to allow for direct comparison to DAT-Cre mice (**Figure S2J-L**).

### **Photostimulation**

Custom-built rigs were used for patterned photostimulation of the olfactory bulb using a DLP projector, as described in detail elsewhere (Dhawale et al., 2010). Appropriate excitation filters (Edmund Optics NT52-532 and NT66-051) and dichroic mirrors (Chroma-530dclp and 460dcsp) were used for ChR2 and NpHR3.0 stimulation. The maximum output light intensity, measured using a power-meter (Thorlabs, PM100D), was maintained stable across all experiments. Photostimulation light masks were designed using custom-written software in Labview (National Instruments). To avoid photoelectric effect, light masks were designed to cover regions excluding the electrode. We confirmed that even at the maximum light intensity used for both ChR2 and NpHR3.0 experiments, there were no non-specific (opsin-independent) effects in wild-type CBA/CAJ mice (**Figure S7**).

### **Extracellular recordings**

Extracellular recordings in the M/T layer of the olfactory bulb were performed using standard procedures. Briefly, gold-plated tetrodes (impedance 0.7-1.0 MOhm) were made by twisting and heat-fusing four  $12.5 \mu\text{m}$  polyimide-coated nichrome wires. Two tetrodes were glued together with Loctite 420 to increase the yield of single units. In several experiments, two

octrodes were used to simultaneously record from two distinct sites within the same hemi-bulb. Electrophysiological signals were amplified (RHA1016, Intan Technologies LLC), band-pass filtered between 300 Hz and 5 kHz and digitized at 30 kHz using a custom-written software in Labview (PCI-6259, National Instruments). Single units were manually isolated using MClust (MClust-3.5, A.D. Redish). For all isolated units, less than 1% of events had inter-spike intervals (ISI) less than 2 ms. Respiration was recorded using piezo-electric stress transducers (Kent Scientific TRN0028) placed under the mouse. All spike-rasters were plotted at 1 ms resolution. Peri-stimulus time histograms (PSTH) for odor-evoked responses were binned at 500 ms and for light-mapping experiments at 50 ms.

### **Slice electrophysiology**

*Animals:* DAT-Cre mice injected with AAV2.9-EF1a-DIO-ChR2-EYFP or crossed with the reporter line Ai32 (ROSA-lox-STOP-lox-ChR2, Allen Institute), and DAT-Cre mice injected with AAV2.9-EF1a-DIO-NpHR3.0-EYFP (see above) were used for optogenetic stimulation and suppression of DAT+ cells, respectively.

*Slice preparation:* P45-P180 mice were anesthetized with an intraperitoneal injection of KX cocktail, after brief exposure to isoflurane. Deeply anesthetized mice were perfused intracardially with ice-cold slicing solution containing (mM): NaHCO<sub>3</sub> 25, NaPO<sub>4</sub> 1.25, KCl 2.5, Choline chloride 110, ascorbic acid 11.6, Na pyruvate 3.1, glucose 25, CaCl<sub>2</sub> 0.5, MgCl<sub>2</sub> 7 (95% O<sub>2</sub>- 5% CO<sub>2</sub>). The animal was decapitated and the olfactory bulbs were carefully extracted and transferred to ice-cold slicing solution. Horizontal slices (300 μm) were cut using a HM 6050V vibratome (Microtom). Slices were incubated in recording solution (see below) at 32° C for 30 minutes, then at 25° C for 30 minutes. Slices were visualized under an upright Olympus microscope equipped with IR-DIC and epi-fluorescence imaging. A 5X MPlan FL objective was used for the structural visualization of the OB and identification of glomerular and mitral cell layers.

*Patch clamp:* Slices were incubated in a recording solution optimized to enhance ET cell intrinsic bursting (**Figure S8D**), containing (mM): NaCl 119, NaHCO<sub>3</sub> 26.2, NaPO<sub>4</sub> 1, KCl 2.5, glucose 22, CaCl<sub>2</sub> 3, MgCl<sub>2</sub> 1 (95% O<sub>2</sub>- 5% CO<sub>2</sub>). Experiments were performed at 30° C. Whole cell recordings were obtained with borosilicate pipettes (4-7 MΩ) filled with intracellular solution containing (mM): Kgluconate 140, KCl 10, Hepes 10, EGTA 0.1, NaCl 6.9, MgATP 4, NaGTP 0.4 (pH 7.3, 290 mOsm). Alexa 594 (14 μM) was added to the intracellular solution for visualizing the neuronal morphology (**Figure 6A**). Voltage values presented in the text are not corrected for the calculated liquid junction potential (-14 mV). Signals were recorded with a Multiclamp 700B (Axon Instruments, Molecular Devices), low-pass filtered at 10 kHz and digitized at 10 kHz with an analog-to-digital converter Digidata 1440A (Axon Instruments, Molecular devices), using Clampex 10.2 software (Axon Instruments, Molecular Devices). The health of the recorded cells was assessed throughout the duration of each experiment by monitoring the spiking output in response to pulses of current injections.

Functional expression of ChR2/NpHR3.0 in DAT+ cells was confirmed by whole cell recording of EYFP-expressing cells in acute bulb slices (**Figure S1E-H**). For optogenetic stimulation of ChR2-expressing DAT+ cells, blue light from a 470 nm LED (CoolLED pE100) was coupled to the microscope in the epi-fluorescence configuration. 1-2 s light pulses were delivered to the slice through a 60X LUMPlan microscope objective, at an output power of 7 mW measured at the exit of the objective. For optogenetic suppression of NpHR3.0-expressing DAT+ cells, red light from two 625 nm LED (Luminus, CBT-40 series) was shone onto the preparation from the side of the objective, at an angle of  $\sim 20^\circ$ . The intensity at the sample was  $\sim 0.8$  mW/mm<sup>2</sup>. DAT+ cells were identified by EYFP fluorescence. Blue or red light stimulation evoked a short latency (<1 ms) inward or outward currents respectively (**Figure S1E-H**). The mitral cell layer was visually identified under IR-DIC by the characteristic laminar organization of cell bodies. ET cells were recognized as pear-shaped ( $\geq 15$   $\mu$ m) cell bodies positioned in the lower half of the glomerular layer with a single apical dendrite confined to a unique glomerulus. 12 of the 21 recorded ET cells displayed spontaneous spiking in cell attached or whole cell recordings. Of these, 6 cells showed a characteristic bursting firing pattern (**Figure S8D**) in cell-attached recordings. For experiments involving pharmacological manipulations, inhibitors of synaptic conductances were perfused into the recording chamber. The following concentrations were used: 2,3-dihydroxy-6-nitro-7-sulfamoyl-benzo[f]quinoxaline-2,3-dione (NBQX) 10  $\mu$ M, D-(-)-2-Amino-5-phosphonopentanoic acid (D-APV) 100  $\mu$ M, picrotoxin 100  $\mu$ M, S-(-)-eticlopride hydrochloride 10  $\mu$ M, 8-Bromo-2,3,4,5-tetrahydro-3-methyl-5-phenyl-1*H*-3-benzazepin-7-ol hydrobromide (SKF83566) hydrobromide 2  $\mu$ M. S-(-)-eticlopride hydrochloride and beta-glycyrrhetic acid were purchased from Sigma Aldrich, all other drugs from Tocris Bioscience.

## Pharmacology

Drugs were superfused over the exposed bulb surface 30 minutes prior to the recording and continuously thereafter. For synaptic block experiments, a cocktail of CNQX (6-cyano-7-nitroquinoxaline-2,3-dione, AMPA receptor antagonist), APV (2*R*-amino-5-phosphonovaleric acid, NMDA receptor antagonist and BMI (Bicuculline methiodide, GABA-a receptor antagonist) or CdCl<sub>2</sub> (a blocker of voltage gated Ca<sup>2+</sup> channels, therefore of synaptic release) was made in cortex buffer each at a concentration of 1mM. In a subset of the synaptic block experiments (**Figure S6C**), along with CNQX, APV and BMI, D1 antagonist SKF83566 hydrobromide and D2 antagonist Sulpiride at 1mM, (TOCRIS, USA) were also added to block dopaminergic transmission. In a different subset of experiments, drugs were washed out by continuous superfusion of cortex buffer (**Figure S6A**).

For DREADDi inactivation experiments (**Figure S5**), Clozapine-N-oxide (CNO) was used as a ligand to activate the modified muscarinic receptor. CNO (Enzo Life Sciences, USA) was diluted in saline to a concentration of 4 mg/ml. CNO was injected intra-peritoneally (IP) at a final concentration of 5-10 mg/Kg of body weight. Post-CNO imaging session started 30 minutes

after the IP injection. For genetic ablation of DAT+ cells (**Figure 7**), 400 ng of diphtheria toxin dissolved in PBS (Sigma, D0564) was administered by intraperitoneal injection.

### **Retrograde labeling of OB outputs with PRV-Cre**

Retrograde labeling was accomplished with the use of a replication and spread-deficient Pseudorabies virus (PRV). We deleted the immediate early gene IE180, rendering the virus incapable of viral gene expression and thus viral replication or trans-neuronal spread while maintaining its ability to infect both local and retrograde neuronal populations. We engineered an IE180 null PRV strain expressing Cre-recombinase under the neuron-specific Synapsin promoter (hSyn). Virus was produced in a packaging cell line, and concentrated (titer  $3.0 \times 10^9$ ) using standard protocols.

The PRV-Cre virus was injected at three sites in the piriform cortex of DAT-Cre X Ai38 (ROSA-LoxP-STOP-LoxP-GCaMP3.0) mice at the following coordinates (x = lateral, y = anterior from Bregma and z = depth from the brain surface).

1. x = 2.5 mm, y = 1.8 mm and z = 4.0 mm.
2. x = 2.0 mm, y = 2.2 mm and z = 3.5 mm.
3. x = 1.5 mm, y = 2.8 mm and z = 3.0 mm.

~300 nl of virus was injected at each site.

This procedure retrogradely infected the output cells of the OB (Mitral/Tufted Cells), resulting in Cre-dependent expression of GCaMP3.0 specifically in the M/T cells. Concomitantly, to express DREADDi in DAT+ cells, we injected AAV2.9-CAG-DIO-hM4Di-mCherry in the OB as described earlier. Akin to previous experiments, this allowed DREADDi expression in DAT+ neurons. The AAV2.9 serotype was chosen to express DREADDi-mCherry in the DAT+ cells given previous results in the lab indicating lack of M/T cell infection. Each imaged brain was fixed, sagittal slices were cut and imaged via widefield epifluorescence and confocal microscopy. We found robust labeling of DREADDi-mCherry in the glomerular layer. Importantly, there was no mCherry expression in M/T cells, thereby ruling out potential leak in the M/T cells (**Figure S5C**). Two-photon imaging of M/T cell bodies was performed as described earlier for the DAT+ cells. After IP injection of CNO (5-10 mg/Kg), we waited for 30 minutes before imaging M/T odor responses for the post-CNO session.

### **Genetic ablation of DAT+ cells by diphtheria toxin**

DAT-Cre or DAT-Cre X Thy1-GCaMP3.0 mice were injected in the OB with AAV-FLEX-DTR-GFP virus (gift from T Jessell and E. Azim, Columbia University, NYC). After 2-3 weeks post injection, either saline or Diphtheria toxin (DT, Sigma) diluted to a final amount of 400 ng in PBS was injected intraperitoneally (Azim et al., 2014). Experiments were performed at least 7 days after the induction with DT. Chronic two photon imaging was performed by implanting windows (~3 mm diameter) over the OB. Animals were imaged on DAY0 (immediately before injecting DT) and 1-2 weeks (DAYS 7-14) subsequently. In some animals,

windows were implanted on DAY 7, 1 week after injection of DT. Data from both conditions were pooled.

### Optical imaging analysis

For each stimulus, a time-averaged image was separately calculated for the air and the odor periods. Baseline subtracted normalized responses (ratio images, dF/F and dR/R) were computed by subtracting the two average images and divided by the average air image. For intrinsic optical signals, the ratio image was spatially filtered, as previously described (Soucy et al., 2009). For both IOI and fluorescence imaging, to facilitate detection of responding glomeruli or cells, the ratio images were analyzed to select regions of interests (ROIs). For the sessions during which both IOI and fluorescence signals were acquired in the same animal, the intrinsic ROIs were used to extract the corresponding DAT+ cell GCaMP3.0.0 responses. In addition, random, glomerular-size ( $\sim 80 \mu\text{m}$ ) ROIs were selected on the OB to quantify the similarity of GCaMP3.0 responses to odors, across the bulb surface. To minimize the contribution of noise to the data, minimum response threshold was set at 1.5 standard deviations from baseline during air period. Average odor response spectra (ORS) were calculated for each ROI to the odors in the panel.

*Basic odor response properties:* For each odor-ROI pair, the signal was first smoothed using a boxcar algorithm (box width - 5 frames) in Igor Pro. For each odor, the spatial spread (**Figure 1I**) of response was calculated by determining the fraction of pixels on the exposed bulb surface that responded above 2 SD from baseline average. For comparison of responses across concentrations (**Figure 1H**), responses were normalized with respect to the response at the lowest nominal dilution for each ROI-odor pair.

*Lifetime Sparseness:* A modified metric from Willmore and Tolhurst (Willmore and Tolhurst, 2001) was used to quantify the extent to which a given unit (glomerulus, random picked glomerular-like ROI, or DAT+ cell body) is modulated by different stimuli (**Figure S2B**). If all stimuli in the panel activate the unit rather uniformly, the lifetime sparseness measure will be close to 0; if only a small fraction of the stimuli activate the unit significantly, this metric will be close to 1.

$$LS_i = 1 - \frac{\left(\sum_{j=1}^m \frac{r_j}{m}\right)^2}{\sum_{j=1}^m \frac{r_j^2}{m}}$$

where:  $m = \text{number of odors}$ ,  $r_j = \text{response of ROI A to odor } j$

$i$  refers to the index of the ROI A, for which lifetime sparseness is calculated.

*Similarity:* To quantify the overlap in response between pairs of ROIs (**Figure 1F** and **2E**), we used as a similarity metric, the uncentered correlation coefficient among their odor response spectra (ORS). Similarity between ROIs A and B:

$$S^{(A,B)} = \frac{\sum_{j=1}^n r_j^{(A)} \cdot r_j^{(B)}}{\sqrt{\sum_{j=1}^n r_j^{(A)} \cdot r_j^{(A)}} \cdot \sqrt{\sum_{j=1}^n r_j^{(B)} \cdot r_j^{(B)}}}$$

where

$r_j^{(A)}$  = response of ROI A to odor j

$r_j^{(B)}$  = response of ROI B to odor j

$n$  = number of odors

*Single-pixel correlation analysis:* We selected glomerular-size ROIs on the exposed bulb surface as well as on the bone. From within each ROI, one single representative pixel was chosen and the normalized change in fluorescence with respect to pre-odor baseline (dF/F) was calculated averaged across repeats. Thus, for each reference pixel, we obtained a response vector of dF/F as a function of time (Reference vector,  $RV_0$ ). Single pixel correlation was calculated as the correlation between  $RV_0$  and the response vector of each pixel in the field of view.

### **Electrophysiology analysis**

*Significant spots – optogenetic mapping of DAT+ cell action:* M/T units were recorded from specific sites while illuminating the bulb surface in a grid of  $130\ \mu\text{m} \times 130\ \mu\text{m}$  blue light spots (**Figure 3A-B**). Individual trials consisted of 500 ms of light stimulation flanked by 500 ms blank periods. Each spot was stimulated 10-15 times. Only the locations corresponding to light spots that significantly changed (‘significant spots’) the firing rate (FR) of the recorded unit in either direction compared to the ‘pre-light’ period (two-sample t-test,  $p < 0.05$ ) were selected for subsequent analyses. The electrode position was extracted from a widefield CCD image and further used to calculate photostimulation distances from the recording site (**Figure 3B-C, S4B, Figure S5B**). Percentage inhibitory spots as a function of distance (**Figure 3C, S4B**) was calculated as the ratio of number of ‘significant spots’ to the total number of stimulated spots at any given distance, with a bin size of  $100\ \mu\text{m}$ . To determine the effect of DAT+ cell activation on M/T firing compared to chance (**Figure S4A**), the distributions of differences in spike counts were calculated across ‘light on’ and ‘pre-light’ periods, as well as across independent sets of randomly shuffled pre-stimulus periods (10,000 times, chance condition). Full width half maximum (FWHM) of a ‘cold-spot’ (**Figure 4D and S5B**) was calculated by fitting a 2D Gaussian distribution centered on the 2D light maps (peak normalized), with the standard deviation (sigma) as the only free parameter. Best fits were obtained using least square error method. FWHM was calculated as 2.35 times the estimated standard deviation of the fit.

*Effect of photostimulating DAT+ cells on odor evoked activation of M/T units:* M/T cell responses to individual odors were recorded using 15 s trials consisting of 5 s of odor presentation flanked by 5 s of air. Inter-trial intervals were varied from 15-45 s with increasing odor concentration to allow complete clearance of residual odor (as indicated by PID measurements). Odor presentations were randomly interleaved with ‘odor + light’ trials, where either a full-field light mask (**Figure 3D-E**) or an arbitrary combinations of glomerular-sized blue light spots (**Figure 3F-G**) were presented along with each odor. Number of spots within each pattern varied between 10 to 16 to match the average number of responsive glomeruli on the bulb surface detected via IOI. Each stimulus was repeated 7 to 10 times. M/T responses to

each odor and its corresponding ‘odor + light’ condition were calculated as the mean FR during the odor (or ‘odor + light’) periods across all repeats (**Figure 3G**). Likewise baseline FR was calculated from the air periods preceding ‘odor’ or ‘odor + light’ conditions across repeats (**Figure S4E**). In addition, for each M/T unit a significance value (p-value) was calculated for every ‘odor’ and ‘odor + light’ pair via a two-sample t-test across the repeats. To detect cell-odor pairs that were significantly modulated by light, the negative logarithm of the p-value was plotted against the logarithm of the fold change in FR between the ‘odor’ and ‘odor + light’ conditions (Volcano plot, **Figure S4F**). Significance threshold was set at  $p = 0.05$ . For **Figure 3D (ii)** and **E**, percent inhibition upon light presentation was calculated with respect to the ‘odor’ condition. All blue light intensities used were normalized to the maximum light intensity used for this set of experiments ( $7.9 \text{ mW/mm}^2$ ) and plotted in the log scale as the values varied over 3 orders of magnitude.

*Halorhodopsin experiments:* To ensure efficient silencing of DAT+ cell bodies and their long processes, full-field light masks were projected excluding the recording electrodes. The odor delivery conditions, trial structure and calculation of average FR during ‘baseline’, ‘odor’ and ‘odor + light’ were identical to the ChR2 odor experiments described above. The firing rates of M/T units were compared across ‘odor’ and ‘odor+light’ conditions and p-value evaluated (**Figure S5**). Change Index (CI) was calculated as  $[(FR_{\text{odor}} - FR_{\text{odor+light}})/(FR_{\text{odor}} + FR_{\text{odor+light}})]$  where,  $FR_{\text{odor+light}}$  and  $FR_{\text{odor}}$  correspond to mean absolute firing rate (spikes/s) of a given cell-odor pair during the odor period in the presence and absence of light stimulation respectively.  $CI > 0$  and  $CI < 0$  respectively indicate suppression and enhancement of firing upon light stimulation, denoting excitatory and inhibitory action of DAT+ cells respectively. Note that CI is bounded by -1 and 1, because we used absolute un-subtracted firing rates. Average CI for all cell-stimuli pairs were plotted as a function of odor-evoked firing rate binned at 2 spikes/s (**Figure 4C**).

*Analysis of effects of pharmacological manipulations for ChR2 light-mapping experiments:* Light mapping conditions were identical to the ChR2 experiments described earlier. For each M/T cell, we identified spots that significantly modulated the FR upon light stimulation during the drug period (two-sample t-test,  $p < 0.05$ ; same as **Figure 3**). For each significant spot, the light induced FR change was compared in the control (pre-drug) and drug condition (**Figure 5B-C**). For a given M/T unit, we calculated the time-course of the light-induced response by computing the mean PSTH across all significant spots (**Figure 5D**). Same analysis was performed for  $\text{CdCl}_2$  and APV-CNQX-BMI cocktail experiments.

### Acute slice experiment analyses

Analysis was performed using the Clampfit software (Axon Instruments Molecular Devices) and custom routines in Matlab. For illustration purpose, recorded traces were *post hoc* low-pass filtered at 1 kHz (digital Butterworth filter, Matlab), and further smoothed by taking a sliding window average with a bin size of 0.5 ms. Before averaging, the baseline (mean value in 1-2 s window preceding light stimulation) was subtracted from individual traces. Few residual spikes in voltage clamp traces (1 ET cell and 1 M/T cell) recorded at -30 and -40 mV were

removed by *post hoc* thresholding. In **Figure 6B-ii** and **6D-ii**, average trace (across repeats) for each cell was normalized by the mean current in the light period in the control condition (before drug addition). The total charge was estimated (for each repeat in each cell) as the time integral of the baseline-subtracted current over the light period (**Figure S1F-H** and **6E**). This value was further corrected for the current divider effect of the series resistance (Wehr and Zador, 2003) by multiplying the current amplitude by the correction factor:  $(R_{in}+R_s)/R_{in}$ , where  $R_s$  is the series resistance and  $R_{in}$  is the input resistance of the cell.  $R_s$  and  $R_{in}$  were estimated at the end of each stimulation protocol (10 trials) by measuring the current response of the cell to a square pulse of -10 mV (average of 10 repeats).  $R_s$  was estimated from the peak current of the fast capacitance transient, while  $R_s+R_{in}$  was estimated from the plateau current at the end of the pulse. Light-induced hyperpolarization was estimated as the average membrane potential during light period, following baseline subtraction (**Figure S1H** and **S8E-iii**).

### **Analyses of population imaging data**

For each stimulus, response strength was calculated as a normalized change in fluorescence with respect to baseline (dF/F) averaged over all repeats. Population response strength was calculated as the mean of the response strengths to a given odor either across all the neurons in a given FOV (**Figure 7C-iii**) or across all neurons pooled from all the FOVs (**Figure 7D**). For each FOV, population response strength was calculated for each odor at 4 different concentrations as mentioned above. This yielded one concentration curve for each FOV-odor pair ( $n = 35$  for both control and +DT). The ‘best-fit-slope’ was calculated by linear regression and the cumulative distribution was plotted for either conditions separately (**Figure 7F**). For each odor stimulus, the neuronal response spectrum (NRS) was defined as a vector containing the response strengths of all the recorded neurons pooled across FOVs. Population sparseness was calculated using the same formula mentioned above, with the index “i” denoting neurons. Mean population sparseness was defined as the mean of the population sparseness values across all odors ( $n = 5$ ) at each concentration (**Figure 7G**). Correlation of the NRS for each odor pair was calculated. The correlation values are plotted either for all the odor pairs at 1:100 dilution ( $n = 10$  pairs, **Figure 7H-i**) or for all the odor pairs across all the concentrations ( $n = 190$  pairs, **Figure 7H-ii**).

### **References**

Azim, E., Jiang, J., Alstermark, B., and Jessell, T.M. (2014). Skilled reaching relies on a V2a propriospinal internal copy circuit. *Nature* 508, 357–363.

Bozza, T., McGann, J.P., Mombaerts, P., and Wachowiak, M. (2004). In vivo imaging of neuronal activity by targeted expression of a genetically encoded probe in the mouse. *Neuron* 42, 9–21.

- Dhawale, A.K., Hagiwara, A., Bhalla, U.S., Murthy, V.N., and Albeanu, D.F. (2010). Non-redundant odor coding by sister mitral cells revealed by light addressable glomeruli in the mouse. *Nat Neurosci* *13*, 1404–1412.
- Soucy, E.R., Albeanu, D.F., Fantana, A.L., Murthy, V.N., and Meister, M. (2009). Precision and diversity in an odor map on the olfactory bulb. *Nat Neurosci* *12*, 210–220.
- Wachowiak, M., Economo, M.N., Díaz-Quesada, M., Brunert, D., Wesson, D.W., White, J.A., and Rothmel, M. (2013). Optical dissection of odor information processing in vivo using GCaMPs expressed in specified cell types of the olfactory bulb. *J. Neurosci.* *33*, 5285–5300.
- Whitesell, J.D., Sorensen, K.A., Jarvie, B.C., Hentges, S.T., and Schoppa, N.E. (2013). Interglomerular lateral inhibition targeted on external tufted cells in the olfactory bulb. *J. Neurosci.* *33*, 1552–1563.
- Willmore, B., and Tolhurst, D.J. (2001). Characterizing the sparseness of neural codes. *Network* *12*, 255–270.